


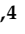


Article

Zircon at the Nanoscale Records Metasomatic Processes Leading to Large Magmatic–Hydrothermal Ore Systems

Liam Courtney-Davies ^{1,*}, Cristiana L. Ciobanu ¹, Max R. Verdugo-Ihl ¹, Ashley Slattery ², Nigel J. Cook ¹, Marija Dmitrijeva ¹, William Keyser ¹, Benjamin P. Wade ², Urs I. Domnick ¹, Kathy Ehrig ³, Jing Xu ^{1,4} and Alkiviadis Kontonikas-Charos ¹

¹ School of Chemical Engineering and Advanced Materials, The University of Adelaide, Adelaide, SA 5005, Australia; cristiana.ciobanu@adelaide.edu.au (C.L.C.); max.verdugoahl@adelaide.edu.au (M.R.V.-I.); nigel.cook@adelaide.edu.au (N.J.C.); marija.dmitrijeva@adelaide.edu.au (M.D.); william.keyser@adelaide.edu.au (W.K.); urs.domnick@adelaide.edu.au (U.I.D.); j.xu@adelaide.edu.au (J.X.); alkiviadis.kontonikas-charos@adelaide.edu.au (A.K.-C.)

² Adelaide Microscopy, The University of Adelaide, Adelaide, SA 5005, Australia; ashley.slattery@adelaide.edu.au (A.S.); benjamin.wade@adelaide.edu.au (B.P.W.)

³ BHP Olympic Dam, Adelaide, SA 5000, Australia; kathy.ehrig@bhp.com

⁴ Key Laboratory of Mineral Resources, Institute of Geology and Geophysics, Chinese Academy of Sciences, Beijing 100029, China; xujing3800@126.com

* Correspondence: liam.courtney-davies@adelaide.edu.au

Received: 30 April 2019; Accepted: 13 June 2019; Published: 16 June 2019



Abstract: The petrography and geochemistry of zircon offers an exciting opportunity to better understand the genesis of, as well as identify pathfinders for, large magmatic–hydrothermal ore systems. Electron probe microanalysis, laser ablation inductively coupled plasma mass spectrometry, high-angle annular dark-field scanning transmission electron microscopy (HAADF-STEM) imaging, and energy-dispersive X-ray spectrometry STEM mapping/spot analysis were combined to characterize Proterozoic granitic zircon in the eastern Gawler Craton, South Australia. Granites from the ~1.85 Ga Donington Suite and ~1.6 Ga Hiltaba Suite were selected from locations that are either mineralized or not, with the same style of iron-oxide copper gold (IOCG) mineralization. Although Donington Suite granites are host to mineralization in several prospects, only Hiltaba Suite granites are considered “fertile” in that their emplacement at ~1.6 Ga is associated with generation of one of the best metal-endowed IOCG provinces on Earth. Crystal oscillatory zoning with respect to non-formula elements, notably Fe and Cl, are textural and chemical features preserved in zircon, with no evidence for U or Pb accumulation relating to amorphization effects. Bands with Fe and Ca show mottling with respect to chloro–hydroxy–zircon nanoprecipitates. Lattice defects occur along fractures crosscutting such nanoprecipitates indicating fluid infiltration post-mottling. Lattice stretching and screw dislocations leading to expansion of the zircon structure are the only nanoscale structures attributable to self-induced irradiation damage. These features increase in abundance in zircons from granites hosting IOCG mineralization, including from the world-class Olympic Dam Cu–U–Au–Ag deposit. The nano- to micron-scale features documented reflect interaction between magmatic zircon and corrosive Fe–Cl-bearing fluids in an initial metasomatic event that follows magmatic crystallization and immediately precedes deposition of IOCG mineralization. Quantification of α -decay damage that could relate zircon alteration to the first percolation point in zircon gives ~100 Ma, a time interval that cannot be reconciled with the 2–4 Ma period between magmatic crystallization and onset of hydrothermal fluid flow. Crystal oscillatory zoning and nanoprecipitate mottling in zircon intensify with proximity to mineralization and represent a potential pathfinder to locate fertile granites associated with Cu–Au mineralization.

Keywords: zircon; IOCG deposits; Olympic Cu–Au Province; HAADF STEM; Fe–Cl-metasomatism; chloro–hydroxy–zircon nanoprecipitates; granite fertility

1. Introduction

Ore deposits falling within the broad iron-oxide-Cu–Au (IOCG) clan are a fascinating, and in some cases, poorly understood, family of magmatic–hydrothermal ore systems (References [1,2] and references therein). Debate on their genesis includes the relative timing and evolution of fluids during transition from the magmatic to hydrothermal stage. Detailed investigation of magmatic accessory minerals at appropriate scales of observation has enabled fluid–mineral interaction to be fingerprinted (e.g., using apatite [3,4]).

Zircon (ZrSiO_4) is a common accessory mineral and has been pivotal for the evolution of U–(Th)–Pb geochronology (References [5] and references therein). Aside from actinides, magmatic zircon will incorporate a range of trace elements (lanthanides, Y, Hf, and Ti) which are valuable tracers for mantle versus crustal origin of melts and for underpinning plate tectonic models during Earth cycles (e.g., [6–8]). Contemporary consensus views the incorporation of other, “non-formula” components in zircon, including Ca, Fe, Al, and H_2O , as being unrelated to primary magmatic processes (Reference [9], and references therein). These are most often measured within altered zircon (e.g., [10]) and are attributed to metamictization-related effects.

In this contribution, we bridge micron- to nanoscale observations to comprehensively characterize magmatic zircon from Proterozoic granites in the eastern Gawler Craton, South Australia (Figure 1A). Iron-oxide copper gold systems of various sizes are found within granites of different ages in the Olympic Cu–Au Province [11], for example, the Olympic Dam deposit [12] and Wirrda Well prospect, hosted by ~1.6 Ga (Hiltaba Suite) and ~1.85 Ga (Donington Suite) granitoids, respectively. The U–Pb age of hydrothermal hematite from Olympic Dam, a product of Fe-metasomatism, has been constrained by isotope dilution-thermal ionization mass spectrometry (ID-TIMS) to 1589.91 ± 0.94 Ma [13], crystallizing roughly 2–4 Ma after zircon within the granite hosting the deposit (chemical abrasion ID-TIMS; 1593.87 ± 0.21 Ma) [14].

The overarching aims of the present work were two-fold. Firstly, we aimed to document metasomatic, fluid-assisted alteration of zircon that occurs in a magmatic–hydrothermal environment prior to structural damage induced by alpha-decay. Secondly, we tested this hypothesis and its implications using samples from metallogenetically productive and unproductive granites of the same suites across the Gawler Craton. We set out to show that micron- to nanoscale observations of zircon geochemistry and crystal structure can, in combination, be used to trace early mineralizing fluids. Furthermore, we provide atomic-scale resolution images of zircon, offering insights into metasomatic processes and products, such as the formation of zircon nanoprecipitates and structural defects.

Such an approach provides potential qualitative indicators of magma fertility (the ability of a magma to generate hydrothermal fluids that are sufficiently well-endowed with Cu, etc., to form a sizable ore deposit). Such an idea is validated by geochemical analysis of known productive and unproductive granites, with a broad application in IOCG exploration across the Gawler Craton and elsewhere.

2. Background and Rationale

2.1. Zircon Chemistry and Structure

Magmatic zircon has a crystal structure resistant to physical and chemical degradation during secondary processes, properties which have motivated research into its usage as a durable host for nuclear waste storage [15]. However, zircon undergoes self-irradiation damage during U–(Th)–Pb decay, ultimately transitioning from crystalline to an amorphous (metamict) state [10], which can be

followed by partial to complete recrystallization. The amorphous domains begin to interconnect due to the radiation damage (α -decay), over a time period determined by U/Th concentrations and annealing rates [16]. The time dependency of structural damage is highly relevant for geochronology, as it can result in discordance of the U–Pb system, most commonly through Pb-loss. Disturbances to zircon U–Pb systematics via metamictization can, however, be selectively eliminated by chemical abrasion of damaged zones, prior to ID-TIMS, permitting high-precision geochronological constraints [17].

The secondary textures commonly observed to crosscut growth zones in magmatic zircon are attributed to re-equilibration of zircon in aqueous fluids and melts (Reference [18] and references therein). Primary oscillatory zoning in zircon can, however, be locally preserved, even in cases when the superimposed reaction temperature exceeds ~ 600 °C [19]. Structural damage can also create pathways for fluids to enter and precipitate minerals as inclusions within zircon displaying secondary microstructures. For example, Fe–Ti oxides and ZrO_2 observed along dislocation and pores in Hadean zircons (Jack Hills, Western Australia) are considered to postdate primary crystallization [20].

Elemental abundance and isotope ratios in zircon, including rare earth element (REE) fractionation patterns and Eu/Eu*, Sr/Y, and V/Sc anomalies, all readily determined by microbeam analysis, can be used to define magma fertility and track its evolution (Reference [21] and references therein). These geochemical pathfinders have been extensively applied to target metallogenically productive (“fertile”) and non-productive (“infertile”) granitic intrusions [22]. Despite the potential for identifying geochemical changes in zircon as a response to metasomatism, the commonly used microanalytical instrumentation, such as laser-ablation inductively-coupled plasma mass-spectrometry (LA-ICP-MS), cannot accurately spatially resolve compositions smaller than a few microns at best, a high threshold relative to typical internal textures and structures commonly found in zircon.

Z-contrast techniques such as high-angle annular dark-field scanning transmission electron microscopy (HAADF STEM; e.g., [23]) allows processes of metamictization and alteration to be addressed down to the nanoscale. For example, fission tracks relating to radiation damage, the nanoscale occurrence of Pb, and evidence for nanoscale U-mobility have been revealed by this technique [24–27]. Increasing levels of spatial resolution and analytical precision combined with in situ micro-sampling techniques have permitted HAADF STEM study of foils prepared by focused ion beam (FIB)-scanning electron microscopy (SEM) to visualize atomic structure and defects in minerals (e.g., [28,29]).

2.2. The Olympic Cu–Au Province

The Olympic Cu–Au Province, South Australia (Figure 1A) hosts IOCG-style mineralization attributed to hydrothermal activity associated with emplacement of the Gawler Silicic Large Igneous Province at ~ 1.6 Ga [11], accompanying the onset of Columbia/Nuna supercontinent breakup [30]. Magmatic activity is represented by the Hiltaba Suite and contemporaneous Gawler Range Volcanics [31]. The ~ 700 km long Olympic Cu–Au Province strikes roughly N–S along the eastern margin of the Gawler Craton from the Mount Woods Inlier in the north, which hosts the Prominent Hill deposit, through Olympic Dam and Carrapateena, to the Moonta and Hillside deposits in the south (Figure 1A). Each major deposit is surrounded by numerous smaller, less explored prospects. Host lithologies range from Gawler Range Volcanics (e.g., Acropolis prospect; Figure 1B), granites of Hiltaba Suite affiliation (e.g., Olympic Dam within Roxby Downs Granite; RDG), or older granitoids (e.g., ~ 1.85 Ga Donington Suite granites at Wirrda Well and Carrapateena; Figure 1A,B).

Several other styles of mineralization occur on the Eyre Peninsula to the immediate west of the Olympic Province. These include older banded iron formations [32] and younger U-mineralization within cover rocks suprajacent to granites belonging to the Samphire Pluton of Hiltaba Suite affiliation [33]. A further Hiltaba Suite granitoid is the Charleston Granite (Figure 1A). No IOCG-style mineralization has yet been discovered associated with either the Charleston Granite or the Samphire Pluton. Donington Suite granitoids are present throughout the Eyre Peninsula and outcrop as far south as Cape Donington, south of Port Lincoln. Although the potential for an extension of the Olympic Cu–Au Province westwards into the Eyre Peninsula remains largely untested, we note that

several of the aforementioned banded iron formation ores feature geochemical signatures suggestive of overprinting by hydrothermal fluids of granitic affiliation [32,34,35].

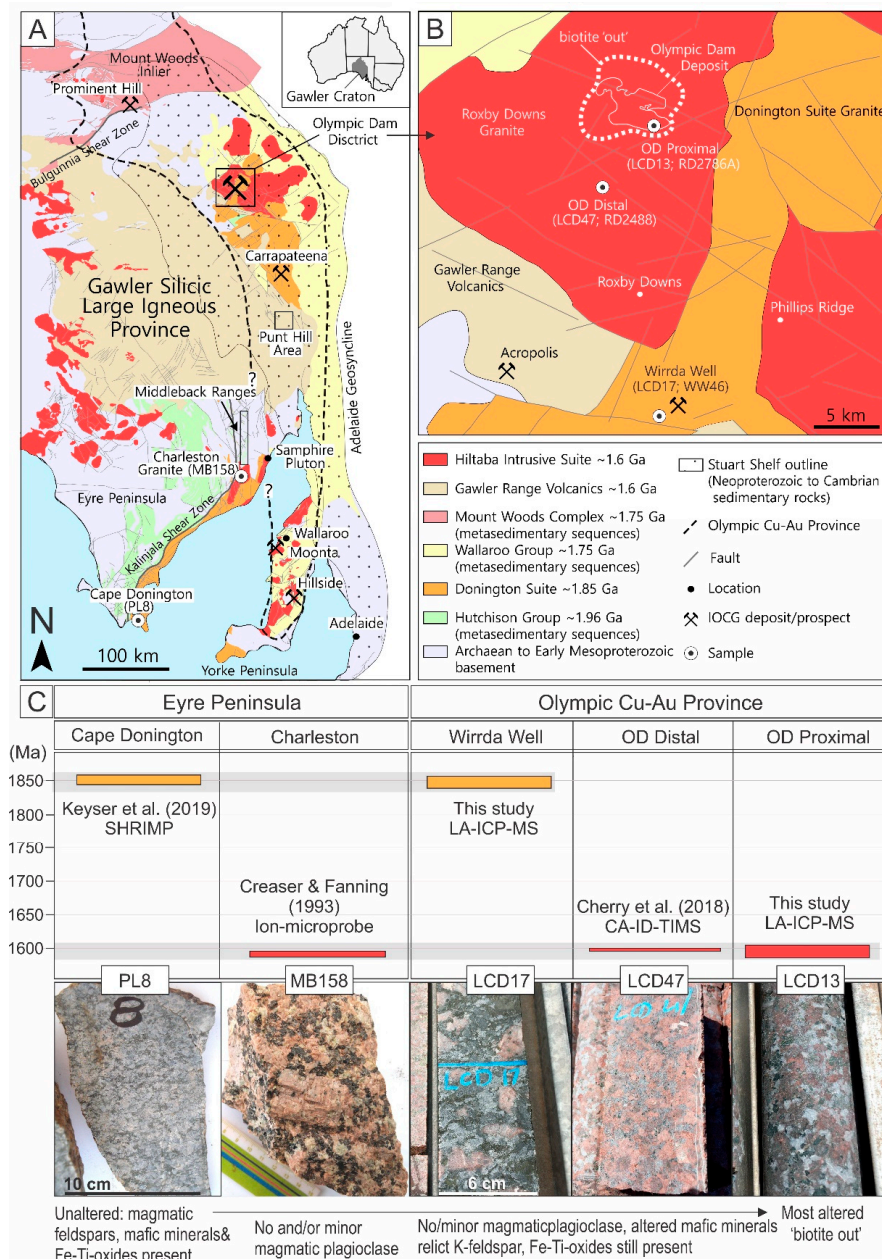


Figure 1. (A) Geological map of the eastern Gawler Craton and (B) the Olympic Dam district; data were taken from the Geological Survey of South Australia (<https://map.sarig.sa.gov.au/>). Locations of the five granite samples addressed in this study and the outline of the Olympic Cu–Au district are marked. (C) Table of ages and corresponding uncertainties (colored bars) for each granite sample studied here, with geochronology conducted either in this study (LA-ICP-MS) or in previous published work as indicated. The orange and red uncertainty bars represent the Donington Suite and Hiltaba Intrusive Suite, respectively, and their location within either the Eyre Peninsula or Olympic Cu–Au Province. Corresponding hand specimen photographs of each sample are shown below the age diagram, indicating degree of granite alteration. References: Keyser et al. (2019) [34]; Creaser and Fanning (1993) [36]; Cherry et al. (2018) [14].

Formation of IOCG deposits remains highly contested, particularly with respect to sources and timing of fluids and contained metals (References [1,2], and references therein). In the Gawler Craton,

lithospheric architecture, mantle metasomatism, and cratonic metallogeny [37,38] have been linked to generic models for IOCG genesis with global applicability [1]. The large volumes of Fe required to form IOCG deposits associated with granitoid-derived fluids or felsic magmatism have recently been proposed to be derived from underplating mafic magma in deeper reservoirs allowing for volatile- and metal-transfer via magma mingling and magnetite flotation [39]. If Fe is sourced from a deep magma reservoir, then zircon, as a ubiquitous magmatic accessory mineral, should record this, either in the magmatic growth stage or as an overprint following interaction with early, low pH hydrothermal fluids released from the locally Fe-enriched magma. Zircon from fertile and barren granitoids should, therefore, differ from one another, both in terms of their geochemical signatures and textures at the micron- to nanoscale.

3. Sample Suite

For this study, we used magmatic zircon from five granitoids of Donington- (~1.85 Ga) and Hiltaba-affiliation (~1.6 Ga) from within and outside the Olympic Cu–Au Province (Figure 1C; Table 1). Except for the example from Cape Donington, all granites considered here displayed macroscopic alteration, albeit to varying degrees, while still retaining granitoid textures and some relict magmatic minerals. The sample suite is summarized in Table 1 with respect to rock type, location, key features, and types of analysis reported in the present contribution.

Zircon from all five case studies were temporally well-constrained by U–Pb methods, either previously published, or given in this study (Figure 1C). We included zircon from RDG samples, collected at locations distal and proximal to the Olympic Dam deposit (Figure 1B), to evaluate whether metasomatic processes analogous to those reported for feldspars [40] and apatite [3] could be tracked. Secondly, we sought to identify whether such processes are recognizable in older zircon from Donington Suite granite hosting the Wirrda Well prospect [41], 25 km SSE of Olympic Dam. Zircon from the Charleston and Cape Donington granites are included to assess the potential of zircon as an indicator of the metallogenic fertility of plutons in the Eyre Peninsula bordering the Olympic Cu–Au Province, where IOCG-style mineralization has not thus far been discovered.

4. Methodology

Four granite samples (3 one-inch polished blocks and one thin-section) and one polished block containing separated zircon (sample PL8) were studied in backscattered electron (BSE) and secondary electron (SE) modes using an FEI Quanta 450 SEM. Cathodoluminescence imaging was undertaken using an FEI Quanta 600 SEM equipped with a tungsten filament electron source. The purpose was to identify zircon grains with representative characteristics, particularly primary growth with oscillatory zoning textures and overprinting thereof. Such grains were analyzed by electron probe microanalysis (EPMA; Cameca SX-Five) and LA-ICP-MS (RESOLUTION-LR excimer laser microprobe coupled to an Agilent 7900x Quadrupole ICP-MS) for minor to trace element and U–Pb compositions using both spot analysis and mapping. All instruments are housed at Adelaide Microscopy, University of Adelaide. Extended details of instrumentation and analytical parameters are provided in Supplementary Materials A. All geochemical data are tabulated in Supplementary Materials B.

For subsequent S/TEM study, seven foils (Table 1; Figure 2A–E, Figure 3B,C, and Supplementary Materials C, Figure S1) were extracted in-situ, thinned to <100 nm by ion beam (Ga⁺) milling and attached to Cu grids on an FEI Helios Nanolab 600 FIB-SEM platform. Of the seven foils, five were cut across oscillatory zonation observed on grain surfaces in zircon to target their development at depth, allowing correlation between micron- and nanoscale characteristics. In the case of the Wirrda Well Donington sample (LCD17), foil preparation targeted areas that yielded concordant (Foil #5) and discordant (Foil #4) U/Pb data points. In the Olympic Dam (OD) distal sample (LCD47), two zircon grains were cut, one with primary oscillatory zoning (Foil #1) and a second grain (Foil #2) displaying secondary, highly altered domains lacking oscillatory zoning.

Table 1. Summary of the samples and foils investigated in this study.

Region	Sample ID	Granite Petrography and Age(s), References	Locality (Drill Hole)	Micron-scale Analysis				Nanoscale Analysis: HAADF STEM Imaging and EDS Spot/Mapping						Figures Showing Zircon Images and Maps
				Analytical Methods			Foil No. (#)	Key Zircon Features			Main Zone Axes Imaged (See Figures 12 and 13)			
				LA-ICP-MS		EPMA Map		NF Element Zoning (STEM Maps)	Mottling/ CHZ-Nano-precipitates	Others				
				U–Pb Dating	Spot Analysis							Map		
Olympic Cu–Au Province	LCD47	HS-Roxby Downs granite [14,40,42], this study	Distal from OD (RD2488)		x		#1	Fe, Ca, Cl	X	screw dislocation	(111)	Figures 2, 8, 10, 11, 14, 15, Supplementary C, Figures S1 and S3		
							#2 *	Fe, Ca, Al, <Cl, Y	x	Xtm veinlet, pores	(001)	Figure 2, Supplementary Figure S3		
	LCD13		Proximal to OD (RD2786A)	x	x		Fe, Cl	#3	Fe, Cl, <Ca	x	Hm inclusions	(001)	Figures 3, 5, 9, Supplementary Figure S3	
	LCD17	DS granite [42,43], this study	Wirrda Well (WW46)	x	x		Fe, Cl	#4	Fe, Ca	x	Xtm veinlet, screw dislocation	(001)	Figures 3, 5, 6, 15, Supplementary Figure S3	
								#5 **	Not mapped	x	Fe detected from spot analysis	[100]; [110]	Figures 3 and 5	
Eyre Peninsula	MB158	HS-Charleston granite [36,44]	South of Middleback Ranges					#6	Fe, Ca, Ti, Al, Y, Th		2-D screw dislocation, fracture U-NP	[001]	Figures 7, 15, Supplementary Figure S1	
	PL8	DS granite [44]	Cape Donington		x	x		#7	None—primary magmatic		stretching defects	[100]; [110]	Figures 2, 15, Supplementary Figure S2	

All samples were characterized by EPMA spot analysis. Sample MB158 for Charleston granite was not analyzed by LA-ICP-MS due to the small size of zircon grains, and particularly the grain from which Foil #6 was extracted (see Figure S1). U–Pb dating was carried out for two samples (including the grains from which the foils were extracted) from locations that were not previously dated. * Foil #2 differs from Foil #1 in containing secondary rather than primary textures. ** Foils #4 and #5 were cut perpendicular and parallel to grain elongation (c-axis), respectively. Upper case X represents the most intense mottling/nanoprecipitates. Abbreviations: CHZ—chloro–hydroxy–zircon; NF—non-formula elements; Hm—hematite; Xtm—xenotime; OD—Olympic Dam; HS—Hiltaba Suite; DS—Donington Suite; U-NP—uranium-bearing nanoparticles.

Nanoscale study, HAADF STEM imaging, and EDS spot analysis/mapping were performed using an ultra-high-resolution, probe-corrected, FEI Titan Themis S/TEM operated at 200 kV. This instrument is equipped with the X-FEG Schottky source and Super-X EDS geometry. The Super-X EDS detector provides geometrically symmetric EDS detection with an effective solid angle of 0.8 Sr. Probe correction delivered sub-Ångstrom spatial resolution and an inner collection angle greater than 50 mrad was used for HAADF experiments using the Fischione HAADF detector.

Diffraction indexing was performed using Winwulff© 1.5.2 software and publicly available data from the American Mineralogist Crystal Structure Database. Crystal structure models were obtained using CrystalMaker® version 10.1.1 and STEM for xHREM™ version 4.1 software.

5. Results

5.1. Zircon Petrography, U–Pb Dating, and Selection of Grains for Nanoscale Study

Screening of zircon populations in each sample shows a range of grain sizes from 30 to ~300 µm, displaying both primary and secondary overprinting textures (Figure 2A–D). Zircons in two samples of unknown age but with assumed affiliation were dated by LA-ICP-MS to confirm their Hiltaba and Donington Suite ages.

Uranium–Pb dating of Wirrda Well zircon (LCD17) produced an upper intercept age of 1848 ± 10 Ma with concordant and highly discordant data points (Figure 3A), corresponding to published Donington Suite ages [43,44]. Dating of the OD proximal zircon (LCD13) gives an upper intercept age of 1572 ± 37 Ma, with analyses displaying both a high degree of concordance and discordancy. Full U–Pb data for analyzed zircons and reference material is tabulated in Supplementary Materials B, Table S3.

Selection of grains for nanoscale study was based upon several criteria: (i) well-constrained U–Pb ages in which case the FIB cut was placed next to a LA-ICP-MS crater (Figure 3); (ii) euhedral morphology with elongation along the *c*-axis; and (iii) large, least-fractured, inclusion-free grains. Subhedral zircon with marginal dissolution was also included to assess the most intense alteration observed within the sample suite (e.g., OD distal zircon; Figure 2B,D). In all five samples, zircon displays crystal oscillatory zoning expressed as bright and dark bands on BSE images (Figures 2 and 3 and Supplementary Materials C, Figure S1A). The intensity contrast of the banding ranged from subtle in zircon in granites from the Eyre Peninsula (PL8 and Charleston; Figure 2E and Supplementary Materials C, Figure S1A) to strong in granites from the Olympic Cu–Au Province. Furthermore, the dark bands could display mottled textures with respect to what appears to be inclusions, varying from sub-micron (in the banding) to ~1–2 µm (in the domains obliterating the zoning) (Figure 2C,D).

Spot EDS-SEM analysis does not show any compositional difference between the “inclusions” and host band/domain suggesting these could instead be pores. However, secondary electron imaging only rarely shows the presence of pores, generally in the scalloped areas with coarser mottled textures. Otherwise, the nature of the sub-micron “inclusions” cannot be resolved with SEM imaging alone.

Except for the Cape Donington sample (PL8; Figure 2E), all grains were fractured to varying degrees and were associated with marginal corrosion and occurrence of darker still domains with irregular and/or scalloped morphologies superimposed on crystal zoning (Figure 2D). Radial fractures, typically interpreted as accompanying metamictization, were present in such cases, notably in the OD distal zircon (Figure 2B,D). Additionally, veinlets and overgrowths of xenotime (Figure 3B), as well as tiny U-bearing phases, were also present in the RDG samples.

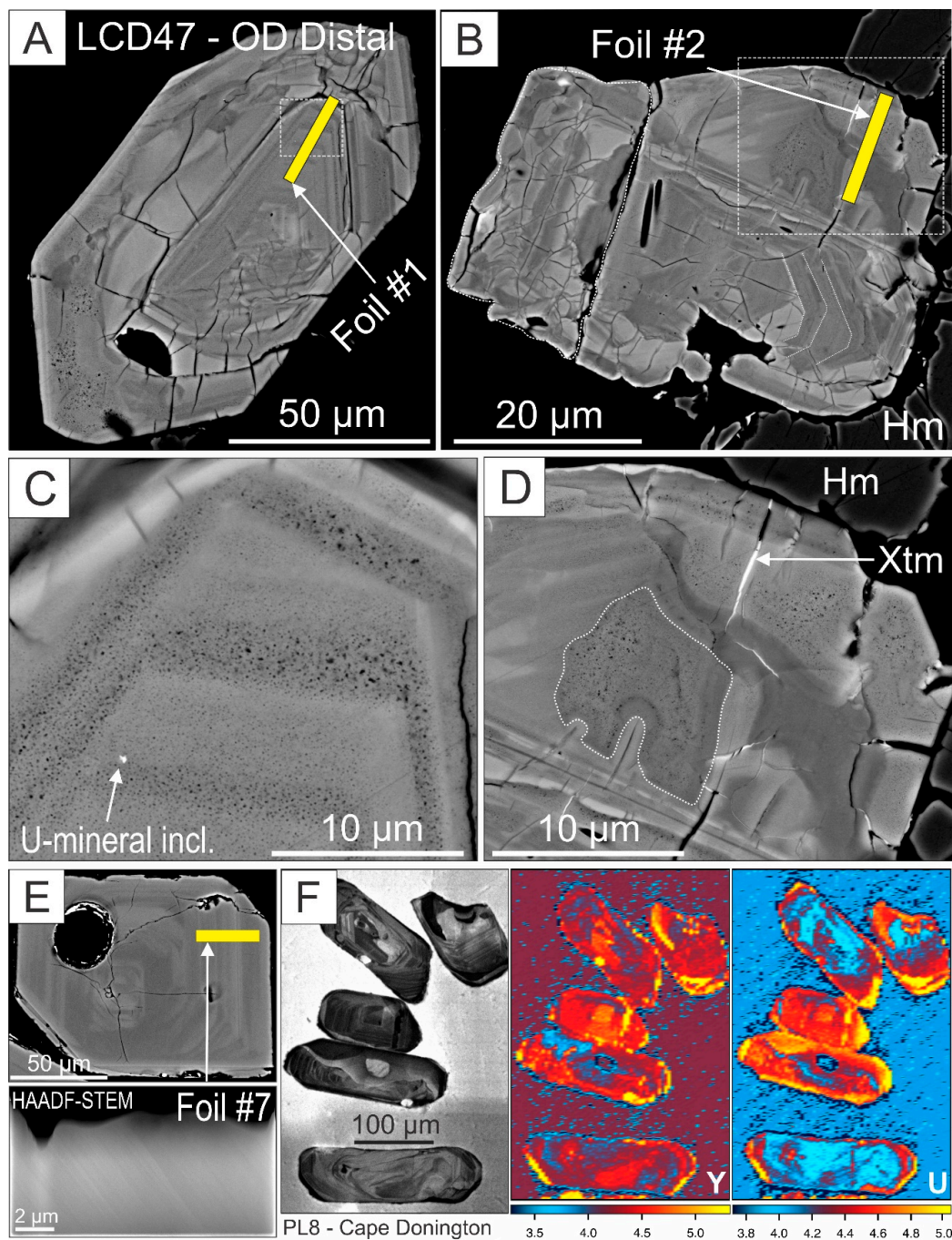


Figure 2. BSE images of grains #1 (A and C) and #2 (B and D) from OD distal zircon (sample LCD47). Note the mottled dark areas were either bands within crystal oscillatory zoning (C) or scalloped domains superimposed onto crystal zoning (D). (E) BSE (top) and HAADF STEM image (bottom) showing crystal oscillatory zoning for Cape Donington zircon (PL8). (F) Cathodoluminescence image (left) and LA-ICP-MS element maps (right) showing oscillatory zoned patterns for Y and U in coarser zircon grains from PL8. Scale in 10^n counts per second (extended maps are given in Supplementary Materials C, Figure S2).

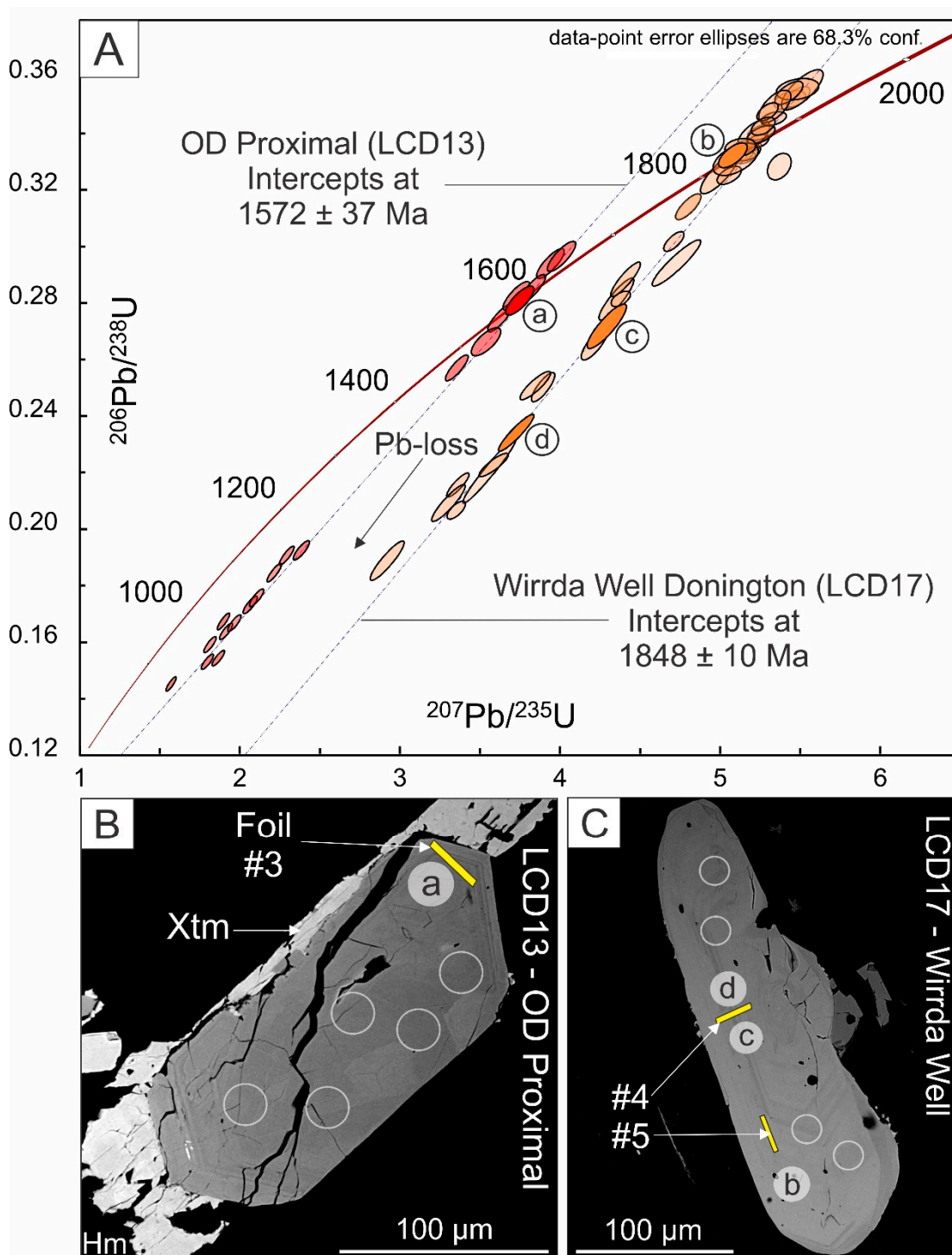


Figure 3. Concordia diagram (A) for OD proximal zircon (LCD13, red ellipses) and Wirrda Well zircon (LCD17, orange ellipses; U–Pb data are presented in Supplementary Materials B, Table S3). Circled letters correspond to LA-ICP-MS craters in BSE images of the dated grains (B and C).

5.2. Trace and Minor Element Concentrations

Electron microprobe datasets for analyzed zircon (Table 2 and Supplementary Materials B, Table S4) showed steady, consistent concentrations of HfO_2 (1.5–2.0 wt.%), Y_2O_3 , $(\text{HREE})_2\text{O}_3$ and P_2O_5 , minor UO_2 , PbO , and ThO_2 in most but not all analyses, and sporadic concentrations of Na_2O , K_2O , CaO , MgO , MnO , and Al_2O_3 above the minimum detection limit (mdl) values across the sample suite. TiO_2

was measured consistently (up to 0.06 wt.%) in the Charleston Granite sample only. Sc_2O_3 was below mdl in most analyses.

“Bright” and “dark” bands in zircon from Cape Donington zircon (PL8) were indistinguishable in terms of composition but the latter had lower analytical totals before recalculation. “Dark” bands in zircon from the Wirrda Well Donington Suite and Charleston Granite samples (LCD17 and MB158) also had totals ~1 wt.% lower than the “bright” bands, generally higher Fe_2O_3 and minor but measurable Cl. Analogous trends were seen in samples the two OD samples (LCD47 and LCD13), in which the “dark” bands contained 1.0–1.9 wt.% Fe_2O_3 and ~0.1 wt.% Cl. Analytical totals were 1–2 wt.% lower than for “bright” bands. Additionally, fluorine was measurable (up to 0.15 wt.%) in a minority of analytical spots from the “dark” bands. Variability of concentrations within each sample, and between “bright” and “dark” bands in the same zircon grain, was a feature of the dataset; the degree of intra-grain variability increased with the total of non-formula elements. Importantly, measured concentrations of Y_2O_3 , $(\text{HREE})_2\text{O}_3$, P_2O_5 , UO_2 , and ThO_2 were statistically identical in “bright” and “dark” bands across the dataset.

Laser ablation inductively coupled plasma mass spectrometry datasets (Supplementary Materials B, Table S5) corroborated and confirmed the accuracy and inherent variability of the EPMA data. Zircon from the Charleston granite was not considered due to the small grain sizes. Other elements (e.g., Sn, Nb, Ta) were not present at concentrations exceeding (at most) a few tens of ppm. Even using a small diameter spot (19 μm), the LA-ICP-MS method did not permit selective analysis of “bright” and “dark” bands.

Cape Donington zircon showed oscillatory patterns correlating with U, Pb, REE, and Y in LA-ICP-MS maps (Figure 2F; Supplementary Materials C, Figure S2). Chondrite-normalized fractionation trends constructed from LA-ICP-MS data (Figure 4A) showed reproducible patterns for zircon in each granite, although with systematic differences in the LREE portion between Donington and Hiltaba Suite samples.

Principal component analysis (PCA) applied to the centered logratio-transformed LA-ICP-MS dataset provided additional insights. A projection of PC1 versus PC2 (Figure 4B,C) showed two distinct groupings: (1) Y, REE (except Eu and Pr) and P; and (2) Hf, U, Pb, Th, Ti, Nb, Eu, and Pr. On both plots, these groupings are distinct from a third group comprising Fe, Mn, Al, and Ca. These patterns underscore interpretation of the EPMA data in which the geochemical signature associated with the metasomatic overprint was defined by Fe, Mn, Al, and Ca, and is independent of any magmatic signature or pattern of distribution at the grain-scale involving element groups (1) and (2). A ternary Fe–Al–Hf diagram (Figure 4D) allows a visual expression of chemical change from least-altered zircon (sample PL8), effectively without Fe or Al, through moderately altered zircon in sample LCD17, to the sub-populations of zircon in samples LCD13 and LCD17 from Olympic Dam, which contained the highest amounts of substituting non-formula (NF) elements.

5.3. Assessment of Zircon Stoichiometry and Substitution Model

Recalculation of EPMA data was undertaken following a template used for hydrogarnet and underlying assumptions/substitutions as provided by Supplementary Materials A. A key objective was an estimation of H_2O content based on allocation of all minor elements (Fe, Al, Mn, and Ca) to structural sites, bringing analytical totals close to 100 wt.% (from ~99.2). The data (Supplementary Materials B, Table S4) showed a correlation between atom per formula unit (apfu) values for $(\text{REY} + \text{Sc})^{3+}$ and P^{5+} on the plot of these two variables (Figure 4E), albeit with a deficiency in the latter—a feature widely described in several publications (see Supplementary Materials A) and taken to indicate more complex substitution mechanisms. Electron microprobe datasets implicitly carry a margin of analytical error, which in the case of the zircon analyzed here were compounded by concentrations of many elements around or below mdl, and by assumptions in the formula calculation that were in turn based on equivocal evidence given in the literature (see Supplementary Materials A). As such, derived stoichiometries and calculated OH contents represent only a best-possible estimation based on the data available.

Nonetheless, using mean compositions and a simplified formulation in which $Zr^* + REE^* + Fe + NF = 1$, where $Zr^* = Zr + Hf + Th + U$; $REE^* = Sc + Y + (La \text{ to } Lu)$; $NF = Mg + Ca + Mn + Nb + Pb + Al$, $B = Si + Al + P + Ti = 1$, and $I = Na + K$ (interstitial), mean compositions (Table 3) can be defined for zircon from the bright and dark bands within each sample.

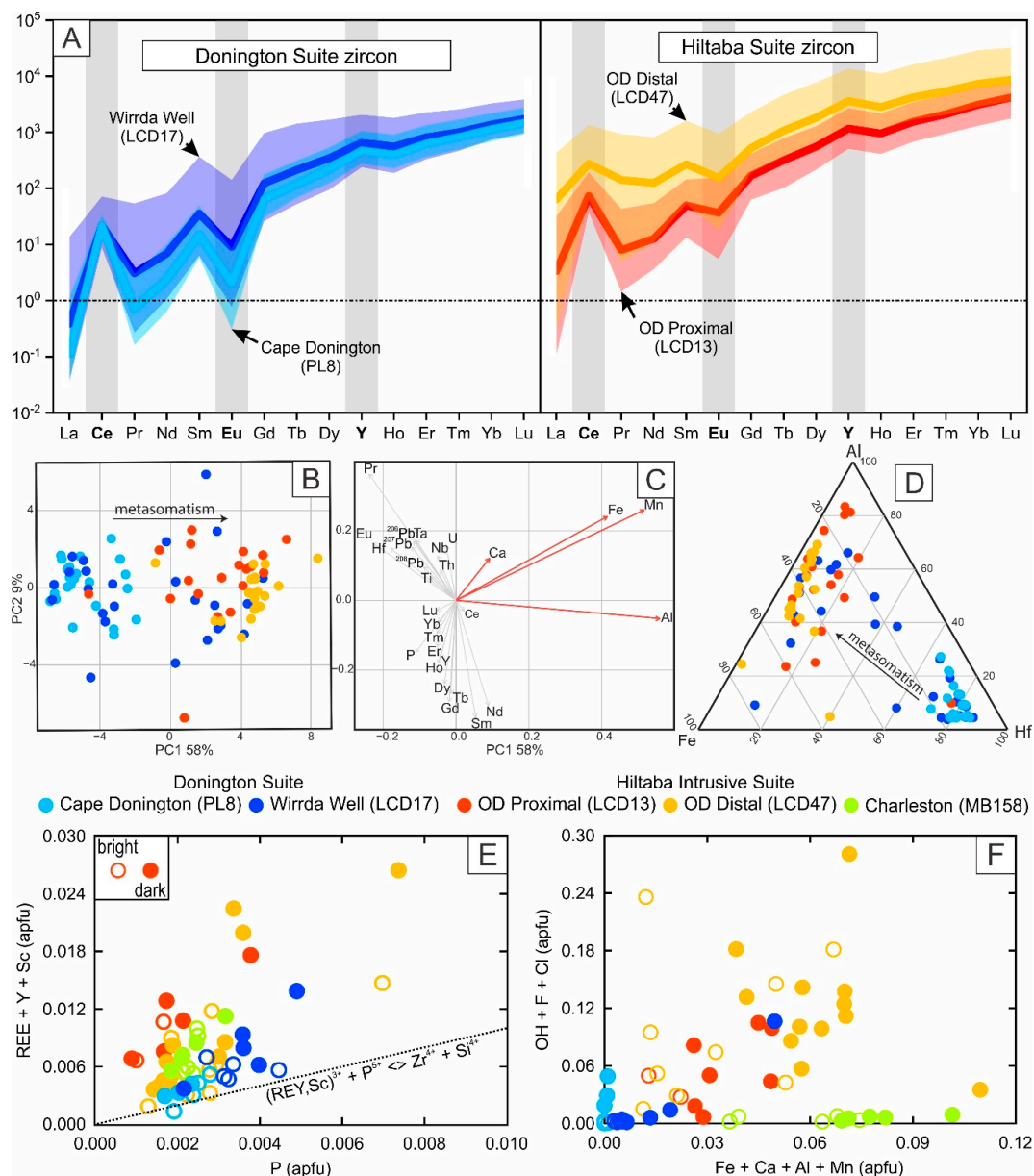


Figure 4. (A) LA-ICP-MS chondrite-normalized REY (REE + Y) fractionation trends for Donington Suite (light and dark blue) and Hiltaba Intrusive Suite (red and orange) samples. (B and C) PCA of LA-ICP-MS data, used to distinguish associated element signatures, and (D) a ternary Fe–Al–Hf diagram demonstrating the degree of zircon metasomatism (LA-ICP-MS data; Supplementary Materials B, Table S5). (E) Plot of $(REY+Sc)^{3+}$ versus P^{5+} (EPMA data). (F) Plot of “non-formula” components $\Sigma(Fe_2O_3 + Al_2O_3 + MnO + CaO)$ versus apfu $\Sigma(OH + Cl + F)$, respectively. The EPMA diagrams illustrate the relationship between substitution of both non-formulae elements and OH in zircon. Open and closed data points represent bright and dark bands in zircon, respectively; color codes correspond to samples in A–D (EPMA data; Supplementary Materials B, Table S4). See main text and Supplementary Materials A for additional explanation.

Table 2. EPMA zircon spot analyses. Gr1: grain 1; Gr2; grain2.

LCD13 (OD Proximal)	Na ₂ O	MgO	Al ₂ O ₃	SiO ₂	P ₂ O ₅	K ₂ O	CaO	TiO ₂	MnO	Fe ₂ O ₃	Y ₂ O ₃	ZrO ₂	HfO ₂	PbO	ThO ₂	UO ₂	Cl	Sum	H ₂ O *	Sum *
Bright	0.046	0.016	<mdl	32.57	0.039	0.011	0.076	0.01	0.035	0.822	0.023	63.834	2.355	0.036	<mdl	0.163	0.116	100.60	0.11	100.69
Bright	0.03	0.011	<mdl	32.165	0.064	<mdl	0.042	0.01	0.037	0.46	0.145	64.104	1.454	0.089	0.08	0.332	0.048	99.640	0.23	99.86
Mean	0.038	0.014	<mdl	32.368	0.052	<mdl	0.059	0.01	0.036	0.641	0.084	63.969	1.905	0.063	<mdl	0.248	0.082	100.12	0.17	100.275
Dark	0.083	0.047	0.011	32.291	0.063	0.011	0.153	0.015	0.029	0.972	0.085	62.507	1.532	0.032	0.078	0.178	0.119	98.599	0.002	98.574
Dark	0.123	0.028	0.41	31.637	0.565	0.031	0.138	0.036	0.117	1.152	1.051	60.714	2.818	0.083	0.09	0.888	0.075	101.254	0.197	101.434
Dark	0.197	0.019	0.186	31.056	0.39	0.017	0.211	0.024	0.11	1.386	0.868	59.613	2.485	0.097	0.073	0.827	0.066	98.842	0.465	99.292
Dark	0.058	0.022	0.008	32.46	0.145	0.007	0.123	0.012	0.049	0.9	0.484	62.749	1.148	0.048	0.196	0.25	0.156	99.547	0.049	99.561
Dark	<mdl	0.021	0.021	32.218	0.082	0.011	0.185	0.008	0.071	0.956	0.12	63.205	1.385	0.048	0.122	0.21	0.379	99.705	0.149	99.769
Dark	0.067	0.013	0.007	31.601	0.034	0.016	0.085	0.008	0.068	0.912	0.029	62.204	2.855	0.048	<mdl	0.203	0.163	98.780	0.353	99.096
Dark	0.064	0.021	0.056	31.239	0.066	0.01	0.381	0.007	0.114	1.161	0.166	60.557	2.049	0.07	0.092	0.742	0.086	97.675	0.438	98.052
Mean	0.099	0.024	0.1	31.786	0.192	0.015	0.182	0.016	0.08	1.063	0.4	61.65	2.039	0.061	0.109	0.471	0.149	99.20	0.236	99.397
LCD47 (OD Distal)	Na ₂ O	MgO	Al ₂ O ₃	SiO ₂	P ₂ O ₅	K ₂ O	CaO	TiO ₂	MnO	Fe ₂ O ₃	Y ₂ O ₃	ZrO ₂	HfO ₂	PbO	ThO ₂	UO ₂	Cl	Sum	H ₂ O *	Sum *
Bright (Gr2)	<mdl	0.017	0.132	31.645	0.113	0.006	0.032	0.043	0.059	0.227	0.317	67.091	1.379	0.03	0.103	0.145	0.008	101.963	1.194	103.156
Bright (Gr2)	0.074	0.023	0.122	31.294	0.072	0.008	0.535	0.024	0.153	1.807	0.211	61.755	1.399	0.042	0.117	0.219	0.076	98.399	0.877	99.259
Mean	<mdl	0.02	0.127	31.47	0.093	0.007	0.284	0.034	0.106	1.017	0.264	64.423	1.389	0.036	0.11	0.182	0.042	100.181	1.036	101.208
Dark (Gr2)	0.036	0.027	0.18	30.965	0.115	0.006	0.427	0.009	0.143	1.44	0.167	61.61	1.402	0.03	0.051	0.111	0.147	97.233	0.651	97.851
Dark (Gr2)	0.046	0.03	0.196	31.273	0.054	0.006	0.435	0.038	0.174	1.333	0.043	61.692	1.736	0.037	0.023	0.12	0.089	97.565	0.467	98.012
Dark (Gr2)	0.059	0.033	0.838	30.827	0.136	0.012	0.792	0.018	0.262	1.948	0.553	58.456	1.225	<mdl	0.089	0.125	0.111	96.520	0.086	96.532
Mean	0.047	0.03	0.405	31.022	0.102	0.008	0.551	0.022	0.193	1.574	0.254	60.586	1.454	0.034	0.054	0.119	0.116	97.106	0.401	97.465
Bright (Gr1)	<mdl	0.011	0.009	33.017	0.11	<mdl	0.01	0.011	<mdl	0.91	0.116	65.951	1.263	0.036	0.036	0.048	0.008	101.641	0.143	101.783
Bright (Gr1)	0.053	0.023	0.09	30.846	0.073	0.006	0.47	<mdl	0.138	1.177	0.113	61.442	1.618	0.04	0.058	0.188	0.099	96.740	0.645	97.335
Bright (Gr1)	0.111	0.032	0.143	31.561	0.266	0.011	0.329	0.007	0.202	1.348	0.486	60.903	1.602	0.042	0.042	0.286	0.066	98.095	0.149	98.193
Bright (Gr1)	<mdl	0.016	0.034	31.791	0.05	0.006	0.015	0.037	0.012	0.496	0.017	65.21	1.247	0.03	0.017	0.051	<mdl	99.214	0.465	99.679
Bright (Gr1)	<mdl	0.012	0.035	32.376	0.086	<mdl	0.024	0.007	0.019	0.381	0.057	65.094	1.416	0.025	0.024	0.037	0.009	99.780	0.072	99.850
Bright (Gr1)	<mdl	0.4	0.447	32.714	0.118	0.006	0.03	0.035	0.03	0.69	0.165	65.902	1.477	0.041	0.027	0.061	0.012	102.467	0.375	102.839
Bright (Gr1)	<mdl	0.02	0.1	32.199	0.108	<mdl	0.033	0.017	0.06	0.4	0.15	65.179	1.394	0.029	0.041	0.052	0.012	100.099	0.253	100.349
Mean	<mdl	0.073	0.123	32.072	0.116	0.007	0.13	0.019	0.077	0.772	0.158	64.24	1.431	0.035	0.035	0.103	0.034	99.719	0.3	100.004
Dark (Gr1)	0.034	0.029	0.467	30.897	0.129	0.014	0.429	0.013	0.214	1.45	0.764	60.699	1.358	0.037	0.074	0.147	0.09	97.673	0.648	98.301
Dark (Gr1)	0.038	0.019	0.027	31.119	0.071	0.007	0.244	0.021	0.132	1.239	0.06	62.206	1.414	0.023	0.035	0.082	0.098	97.233	0.613	97.823
Dark (Gr1)	0.023	0.027	0.214	31.359	0.072	0.006	0.455	0.048	0.163	1.175	0.159	61.716	1.448	0.029	0.053	0.116	0.122	97.660	0.386	98.018
Dark (Gr1)	0.028	0.02	0.228	31.43	0.067	0.008	0.434	0.01	0.145	1.909	0.138	61.736	1.232	0.019	0.055	0.094	0.125	98.030	0.58	98.582
Dark (Gr1)	0.032	0.03	0.216	31.454	0.064	0.008	0.374	0.077	0.186	1.666	0.081	61.894	1.405	0.017	0.035	0.105	0.085	98.014	0.462	98.457
Dark (Gr1)	0.067	0.021	0.159	31.781	0.069	<mdl	0.442	0.006	0.171	1.413	0.087	62.024	1.258	0.025	0.042	0.085	0.065	98.042	0.232	98.233
Dark (Gr1)	0.098	0.028	0.262	31.635	0.288	0.014	0.512	0.029	0.189	1.74	0.937	60.734	1.349	0.032	0.101	0.276	0.067	99.357	0.468	99.748
Dark (Gr1)	0.06	0.039	0.335	30.747	0.061	0.009	0.478	0.083	0.191	1.774	0.094	63.446	1.476	0.038	0.03	0.134	0.069	99.311	1.397	100.692
Dark (Gr1)	0.094	0.023	0.073	30.481	0.12	<mdl	0.28	0.008	0.143	0.968	0.252	62.081	1.27	0.035	0.059	0.082	0.124	96.452	0.843	97.267
Mean	0.053	0.026	0.22	31.211	0.105	0.009	0.405	0.033	0.17	1.482	0.286	61.837	1.357	0.028	0.054	0.125	0.094	97.975	0.625	98.569

Table 2. Cont.

MB158 (Charleston)		Na ₂ O	MgO	Al ₂ O ₃	SiO ₂	P ₂ O ₅	K ₂ O	CaO	TiO ₂	MnO	Fe ₂ O ₃	Y ₂ O ₃	ZrO ₂	HfO ₂	PbO	ThO ₂	UO ₂	Cl	Sum	H ₂ O	Sum *	
Bright	n = 5	<mdl	<mdl	0.036	33.001	0.099	0.008	0.175	0.04	0.129	1.292	0.224	65.185	1.353	0.051	0.148	0.13	0.016	102.381	0.032	102.41	
Bright		0.032	0.016	<mdl	31.708	0.092	<mdl	0.674	0.052	0.188	2.082	0.147	63.283	1.32	0.049	0.081	0.12	0.046	100.153	0.005	100.147	
Bright		0.058	0.007	0.02	31.93	0.087	0.007	0.66	0.06	0.087	1.704	0.108	63.229	1.393	0.046	0.042	0.107	0.034	99.980	0	99.973	
Bright		0.048	0.053	0.164	32.152	0.096	0.005	0.933	0.031	0.144	1.224	0.273	62.378	1.536	0.038	0.038	0.154	0.063	99.842	0.022	99.85	
Bright		0.033	0.012	0.013	32.399	0.083	0.007	0.253	0.027	0.175	1.02	0.114	64.156	1.524	0.036	0.038	0.148	0.016	100.366	0.005	100.368	
Mean		0.043	0.022	0.058	32.238	0.091	0.007	0.539	0.042	0.145	1.464	0.173	63.646	1.425	0.044	0.069	0.132	0.035	100.544	0.013	100.55	
Dark		0.044	0.019	0.035	31.646	0.095	0.007	1.115	0.029	0.133	1.784	0.206	62.498	1.21	0.057	0.124	0.143	0.06	99.657	0.016	99.659	
Dark		0.04	0.016	0.073	32.077	0.124	<mdl	1.399	0.055	0.153	2.203	0.355	61.528	1.16	0.045	0.232	0.147	0.064	100.175	0.029	100.189	
Dark		<mdl	0.016	0.013	31.92	0.082	<mdl	0.677	0.064	0.176	2.211	0.19	62.89	1.375	0.032	0.121	0.16	0.047	100.293	0.024	100.306	
Dark		0.062	0.012	0.01	31.372	0.07	<mdl	0.981	0.014	0.219	1.306	0.102	61.879	1.397	0.036	0.046	0.15	0.052	98.0480	0	98.037	
Dark	0.033	0.017	0.083	31.403	0.081	0.007	1.033	0.014	0.163	1.281	0.113	61.841	1.523	<mdl	0.084	0.154	0.049	98.317	0.014	98.32		
Mean	n = 5	0.045	0.016	0.043	31.684	0.09	<mdl	1.041	0.035	0.169	1.757	0.193	62.127	1.333	0.043	0.121	0.151	0.054	99.298	0.017	99.302	
PL8 (Cape. Don)		Na ₂ O	MgO	Al ₂ O ₃	SiO ₂	P ₂ O ₅	K ₂ O	CaO	TiO ₂	MnO	Fe ₂ O ₃	Y ₂ O ₃	ZrO ₂	HfO ₂	PbO	ThO ₂	UO ₂	Cl	Sum	H ₂ O *	Sum *	
Bright	n = 4	<mdl	0.008	<mdl	32.518	0.107	<mdl	<mdl	0.005	<mdl	<mdl	0.15	65.716	1.233	0.023	0.027	0.035	<mdl	100.06	0.012	100.071	
Bright		<mdl	0.01	0.008	32.801	0.092	<mdl	<mdl	0.007	0.012	0.026	0.039	65.94	1.392	0.019	0.015	0.021	<mdl	100.589	0.003	100.592	
Bright		<mdl	<mdl	<mdl	32.646	0.097	<mdl	0.01	<mdl	<mdl	<mdl	0.075	65.891	1.275	0.038	0.03	0.064	<mdl	100.396	0.009	100.405	
Bright		<mdl	<mdl	<mdl	32.759	0.074	<mdl	<mdl	0.012	<mdl	<mdl	0.034	65.863	1.334	0.026	0.02	0.045	<mdl	100.249	0	100.249	
Mean		<mdl	<mdl	<mdl	32.681	0.093	<mdl	<mdl	0.008	<mdl	<mdl	0.075	65.853	1.309	0.027	0.023	0.041	<mdl	100.324	0.006	100.329	
Dark		<mdl	0.009	<mdl	31.997	0.077	<mdl	<mdl	0.01	<mdl	0.032	0.028	65.14	1.326	0.03	<mdl	0.012	<mdl	98.907	0.142	99.049	
Dark		<mdl	0.008	<mdl	32.423	0.09	<mdl	<mdl	0.006	<mdl	<mdl	0.038	65.806	1.41	<mdl	<mdl	0.016	<mdl	100.114	0.092	100.206	
Dark		<mdl	<mdl	<mdl	32.005	0.065	<mdl	<mdl	0.008	<mdl	0.041	0.025	65.502	1.326	0.023	<mdl	0.015	<mdl	99.233	0.239	99.472	
Mean		n = 3	<mdl	0.009	<mdl	32.142	0.077	<mdl	<mdl	0.008	<mdl	0.037	0.03	65.483	1.354	0.027	<mdl	0.014	<mdl	99.418	0.158	99.576
LCD17 (Wirrda Well)		Na ₂ O	MgO	Al ₂ O ₃	SiO ₂	P ₂ O ₅	K ₂ O	CaO	TiO ₂	MnO	Fe ₂ O ₃	Y ₂ O ₃	ZrO ₂	HfO ₂	PbO	ThO ₂	UO ₂	Cl	Sum	H ₂ O *	Sum *	
Bright	n = 5	<mdl	0.011	<mdl	32.758	0.104	<mdl	0.018	0.006	<mdl	0.197	0.093	64.529	1.288	0.031	0.026	0.051	<mdl	99.548	0.021	99.568	
Bright		<mdl	0.013	<mdl	32.77	0.172	<mdl	<mdl	0.009	<mdl	0.161	0.108	64.598	1.265	0.028	0.027	0.048	<mdl	99.515	0.006	99.521	
Bright		<mdl	0.012	<mdl	32.874	0.125	<mdl	<mdl	0.008	<mdl	0.128	0.092	65.057	1.343	0.034	0.027	0.045	0.009	99.970	0.007	99.975	
Bright		<mdl	<mdl	<mdl	32.789	0.121	<mdl	<mdl	0.01	<mdl	0.236	0.083	65.159	1.389	0.034	0.025	0.047	<mdl	100.179	0.009	100.188	
Bright		<mdl	0.015	<mdl	32.735	0.129	0.007	0.012	0.006	<mdl	0.105	0.089	65.159	1.31	0.019	0.031	0.059	<mdl	100.028	0.013	100.041	
Mean		<mdl	0.013	<mdl	32.785	0.13	<mdl	<mdl	0.008	<mdl	0.165	0.093	64.9	1.319	0.029	0.027	0.05	<mdl	99.848	0.011	99.859	
Dark		0.027	0.031	0.22	31.317	0.188	0.008	0.26	0.014	0.085	1.338	0.368	62.109	1.282	0.038	0.066	0.108	0.081	98.193	0.498	98.673	
Dark		0.036	0.017	<mdl	32.724	0.138	0.006	0.046	0.006	0.038	0.471	0.202	63.7	1.383	<mdl	0.05	0.077	0.052	99.383	0.016	99.388	
Dark		0.035	0.013	<mdl	32.421	0.139	0.007	0.029	0.008	0.042	0.743	0.112	64.242	1.334	0.03	0.033	0.081	0.027	99.775	0.062	99.831	
Dark		<mdl	0.010	<mdl	33.089	0.084	0.007	0.01	0.009	<mdl	0.272	0.053	65.846	1.245	0.026	<mdl	0.037	<mdl	100.893	0.006	100.9	
Dark	<mdl	0.008	<mdl	32.259	0.152	<mdl	0.011	0.006	0.012	0.162	0.116	64.684	1.204	0.034	0.016	0.054	<mdl	99.062	0.011	99.072		
Mean	n = 5	0.033	0.016	<mdl	32.362	0.140	0.007	0.071	0.009	0.044	0.597	0.17	64.116	1.29	0.032	0.041	0.071	0.053	99.461	0.119	99.573	
average mdl		0.023	0.007	0.006	0.021	0.010	0.005	0.009	0.004	0.011	0.024	0.008	0.049	0.101	0.014	0.010	0.011	0.007				

Sum *: Sum of element totals including calculated H₂O (H₂O*) and corrected for F and Cl. Sc, Nb, and F were measured but are generally below the mdl. Full values for these elements and REY elements are included in Supplementary Materials B, Table S4. Formulae calculation values and α -decays/mg values are in Supplementary Materials B, Table S4.

Table 3. Mean zircon compositions in bright and dark bands in each studied sample.

Lithology and Location	Sample ID	Zircon Composition
Cape Donington, Donington Suite	PL8	Bright: $(\text{Zr}^{*}_{0.994}\text{REE}^{*}_{0.001})_{\Sigma=0.995}(\text{Si}_{1.002}\text{P}_{0.002}\text{O}_4)$; Dark: $(\text{Zr}^{*}_{0.996}\text{Fe}_{0.001}\text{REE}^{*}_{0.003})_{\Sigma=1}(\text{Si}_{0.986}\text{P}_{0.002}\text{O}_{3.95})(\text{OH})_{0.049}$.
Wirrda Well, Donington Suite	LCD17	Bright: $\text{Zr}^{*}_{0.979}\text{Fe}_{0.004}\text{REE}^{*}_{0.006}\text{NF}_{0.001})_{\Sigma=0.989}(\text{Si}_{1.006}\text{P}_{0.005}\text{O}_{3.966})(\text{OH})_{0.001}$; Dark: $i_{0.002}(\text{Zr}^{*}_{0.943}\text{Fe}_{0.031}\text{REE}^{*}_{0.014}\text{NF}_{0.013})_{\Sigma=1}(\text{Si}_{0.962}\text{Al}_{0.008}\text{P}_{0.005}\text{O}_{3.862})(\text{OH,Cl})_{0.106}$.
OD-distal Hiltaba Suite	LCD47	Bright: $(\text{Zr}^{*}_{0.986}\text{Fe}_{0.009}\text{REE}^{*}_{0.003}\text{NF}_{0.002})_{\Sigma=1}(\text{Si}_{0.993}\text{Al}_{0.001}\text{P}_{0.002}\text{O}_{3.978})(\text{OH,Cl})_{0.015}$; Dark: $i_{0.004}(\text{Zr}^{*}_{0.934}\text{Fe}_{0.04}\text{REE}^{*}_{0.004}\text{NF}_{0.022})_{\Sigma=1}(\text{Si}_{0.915}\text{Al}_{0.012}\text{P}_{0.002}\text{Ti}_{0.002}\text{O}_{3.672})(\text{OH,Cl})_{0.281}$.
OD-proximal Hiltaba Suite	LCD13	Bright: $i_{0.003}(\text{Zr}^{*}_{0.97}\text{Fe}_{0.019}\text{REE}^{*}_{0.007}\text{NF}_{0.004})_{\Sigma=1}(\text{Si}_{0.993}\text{P}_{0.001}\text{O}_{3.959})(\text{OH,Cl})_{0.028}$; Dark: $i_{0.004}(\text{Zr}^{*}_{0.942}\text{Fe}_{0.027}\text{REE}^{*}_{0.013}\text{NF}_{0.018})_{\Sigma=1}(\text{Si}_{0.972}\text{Al}_{0.002}\text{P}_{0.002}\text{O}_{3.864})(\text{OH,F,Cl})_{0.105}$.
Charleston Granite, Hiltaba Suite	MB158	Bright: $(\text{Zr}^{*}_{0.962}\text{Fe}_{0.019}\text{REE}^{*}_{0.009}\text{NF}_{0.009})_{\Sigma=0.999}(\text{Si}_{0.985}\text{Al}_{0.001}\text{P}_{0.003}\text{Ti}_{0.001}\text{Fe}_{0.01}\text{O}_{3.969})(\text{OH,Cl})_{0.007}$; Dark: $i_{0.003}(\text{Zr}^{*}_{0.941}\text{Fe}_{0.009}\text{REE}^{*}_{0.009}\text{NF}_{0.041})_{\Sigma=1}(\text{Si}_{0.964}\text{Al}_{0.001}\text{P}_{0.003}\text{Fe}_{0.031}\text{O}_{3.933})(\text{OH,Cl})_{0.006}$.

Note: All granite samples, with the exception of PL8, show various degrees of alteration (see above). The presented compositions are for grains that were micro-sampled for S/TEM analysis. * To obtain a good stoichiometry between the A and B sites, we used a slightly modified procedure for calculating the formulae of the Charleston zircon, in which Fe was allocated in both A and B sites.

The lack of Fe or other non-formula elements and Cl is of note in the Cape Donington zircon, implying these elements were not of magmatic origin. The relatively high OH content in these otherwise less altered zircons may be an artefact of the calculation rather than real and lies within analytical precision of the EPMA method. Critical for the narrative of this contribution, zircon from all three altered granites from the Olympic Cu–Au Province (two of Hiltaba age, one of Donington age) display concomitant enrichment in Fe and other NF elements and in (OH, Cl, F) in the darker bands and over those in unaltered zircon (PL8), in full agreement with the nanoscale observations. Concentrations of other minor (magmatic) elements remain unchanged (within analytical error).

A plot of the main “non-formula” components, and Fe versus OH + Cl + F (Figure 4F) showed a strong correlation for all altered zircon, except Charleston. Mean compositions and empirical formulae for each sub-population are given in Supplementary Materials B, Table S4.

5.4. Distribution of Minor Elements: Micron- to Nanoscale Patterns

The presence of Fe and Cl in zircon was also assessed by EPMA mapping of zircon in two samples: Wirrda Well (LCD17) and OD-proximal (LCD 13). The maps show excellent positive correlation between the two elements in the crystal zoning of Wirrda Well zircon (Figure 5A,B) but antipathetic patterns for OD proximal zircon (Figure 5C,D). The OD proximal zircon displays a combination of primary and overprinting textures in which the oscillatory zoning is only preserved on the rims, whereas the middle part of the grain is affected by fractures and re-crystallization obliterating primary zoning (Figures 3B and 5C,D).

Imaging in HAADF STEM mode depicts oscillatory zoning as bright and dark bands relating to non-formula elements in all foils shown in this study (Table 1), except the Cape Donington zircon (Foil #6). Superimposed mottled textures in the darker bands were only observed in zircon from the Olympic Cu–Au Province. Mapping using STEM EDS showed Fe banding in all zircons except Cape Donington. In the latter, the oscillatory zoning was related to trace elements typical of magmatic zircon (REY, actinides), the concentrations of which were below the detection limits of the EDS STEM method but readily mappable by LA-ICP-MS (Figure 2F; Supplementary Materials C, Figure S2). In contrast, the Wirrda Well–Donington zircon displayed an excellent correlation between micron and nanoscale oscillatory zoning patterns with respect to Fe, as shown by both EPMA and STEM EDS mapping (Figure 5A,B and Figure 6). The Fe distribution, however, did not reveal the mottled texture in the darker Fe-rich bands or veinlets crosscutting the brighter bands, as observed in the HAADF STEM images (Figure 6C).

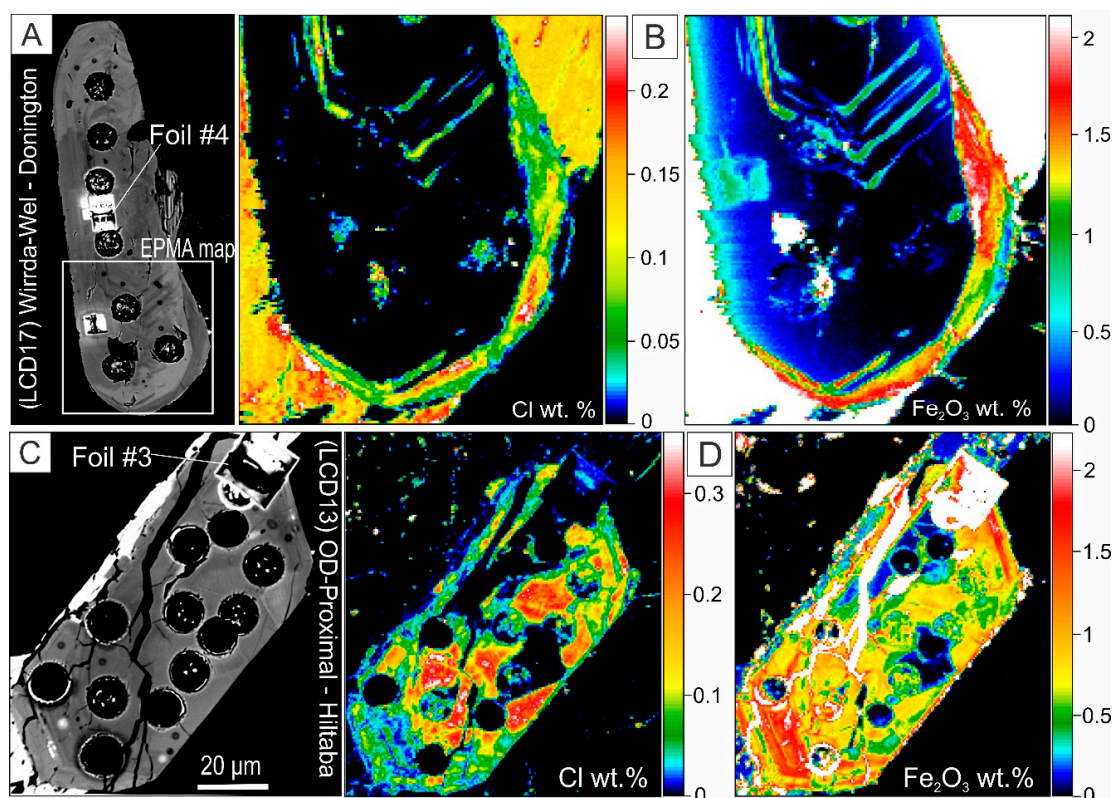


Figure 5. (A) BSE image of oscillatory-zoned Wirrda Well–Donington Suite zircon (sample LCD17) that was dated (LA-ICP-MS craters) and used for nanoscale study (foil location as marked). (B). EPMA maps for Cl and Fe₂O₃ (in wt.%), showing that both elements appear homogeneously enriched and positively correlated with one another within oscillatory bands. (C,D) BSE image and EPMA maps for Cl and Fe₂O₃ (wt.%) of OD proximal zircon (sample LCD 13; foil marked at the top). Note the high concentrations of both elements within the middle part which was affected by fractures and re-crystallization. In contrast, crystal zoning on the rim shows inverse correlation between the two elements (e.g., banding intersecting the FIB cut).

The most varied chemistry mapped at the nanoscale was observed in zircon from the Charleston Granite (Figure 7A). Banding with respect to Fe, Ca, Ti, Al, Y, and Th was recorded outside of a magmatic domain, itself defined by faint oscillatory banding expressed by variation in major element concentration as shown by O, Si, and Zr maps. No mottled textures were present throughout such chemically complex bands. The EDS STEM maps also showed that Fe displayed a sharp boundary against the magmatic domain, contrasting with the diffuse boundaries shown by the other trace elements. All these elements, including U (but not Pb), were enriched within a fracture around the magmatic domain, and within a fine particle inclusion hosted at the diffuse boundary (Figure 7A). The fracture, leading towards this U-bearing fine particle, was represented by a rectangular network of dark nanodomains that hosted pores (Figure 7B–D). These domains were nonetheless crystalline, albeit disordered and with slightly different orientation relative to one another and to host zircon.

The best example of mottled textures throughout oscillatory banding with respect to Fe (Ca, Cl) was shown by the least altered grain in OD distal zircon (Foil #1; Figure 8A). The HAADF STEM image of the foil mimics the BSE image (Figure 2A,C) with respect to the mottled textures throughout the banding. Relative to the generally homogenous distribution of Fe and Ca throughout a given band, the Cl map shows distinct spots of higher concentration. This was exemplified by the signals for Ca and Cl along a profile (Figure 8B). Likewise, variable correlations were seen between the high Cl areas and concentration of major elements, O and Zr, as shown on the EDS STEM maps obtained from mottled areas (Figure 8C). The highly altered zircon grain (Foil #2) showed two distinct domains:

(i) weakly-banded and mottled and (ii) cleaner domains that were strongly enriched in Ca, Fe, and Al. The latter surrounds veinlets of xenotime displaying enrichment in HREE and U (Supplementary Materials C, Figure S3).

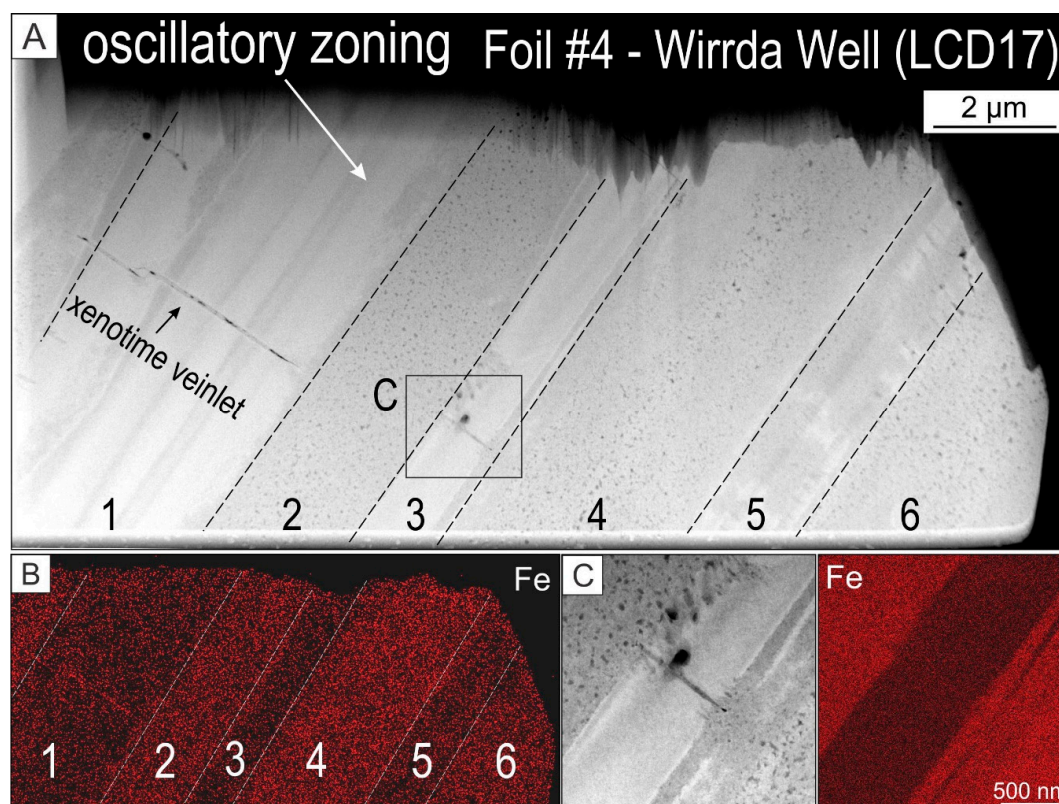


Figure 6. (A) HAADF STEM images (A and C) and EDS STEM maps for Fe (B and D) for Wirrda Well-Donington zircon showing crystal oscillatory zoning (A and B). The dark bands (even numbers) were enriched in Fe and show mottled texture in the image, but not on the Fe map (B). Note that the oscillatory banding was crosscut by a xenotime-bearing veinlet (extended map shown in Supplementary Materials C, Figure S3). (C,D) Higher resolution maps showing the interface between light and dark bands confirmed that the mottled texture (C) was not reflected in the Fe distribution (D).

Olympic Dam proximal zircon (Foil #3) displayed a combination of primary and overprinting textures correlating with minor trace element patterns (Figure 9). In depth, the foil revealed a subsurface 5 µm-diameter inclusion of hematite (Figure 9B–D), as well as oscillatory banding with mottled textures of variable density. As in the OD distal zircon, Fe was evenly distributed throughout the bands, whereas Cl appeared more heterogeneous (Figure 9E,F). In detail, the Fe-poor bands were crosscut by Fe-rich veinlets (Figure 9F). The largest areas of Cl-enrichment were observed in parts of the Fe-rich bands but typically did not correspond to the crosscutting Fe-rich trails. Such patterns of Fe and Cl explain the inverse trends mapped at the micron-scale in the same grain (Figure 5C,D).

5.5. Mottled Areas: Nanoparticles to Fine Particles of Chloro-Hydroxy-Zircon

The nature of the mottled areas (identified in foils as listed in Table 1) relative to Cl-enrichment and substitution mechanisms for zircon was addressed by EDS spot analysis and mapping at various resolutions (Figures 10 and 11). Higher resolution maps of one Cl-rich area selected from Figure 8C reproduced the same variability between major elements and Cl (and remarkably little variation in terms of minor elements) in the particles observed as dark nanodomains on HAADF STEM image (Figure 10A). An inverse correlation between O and Zr corresponded to either diffuse or stronger Cl concentration, whereas the strongest Cl concentrations were not reflected by major element variation.

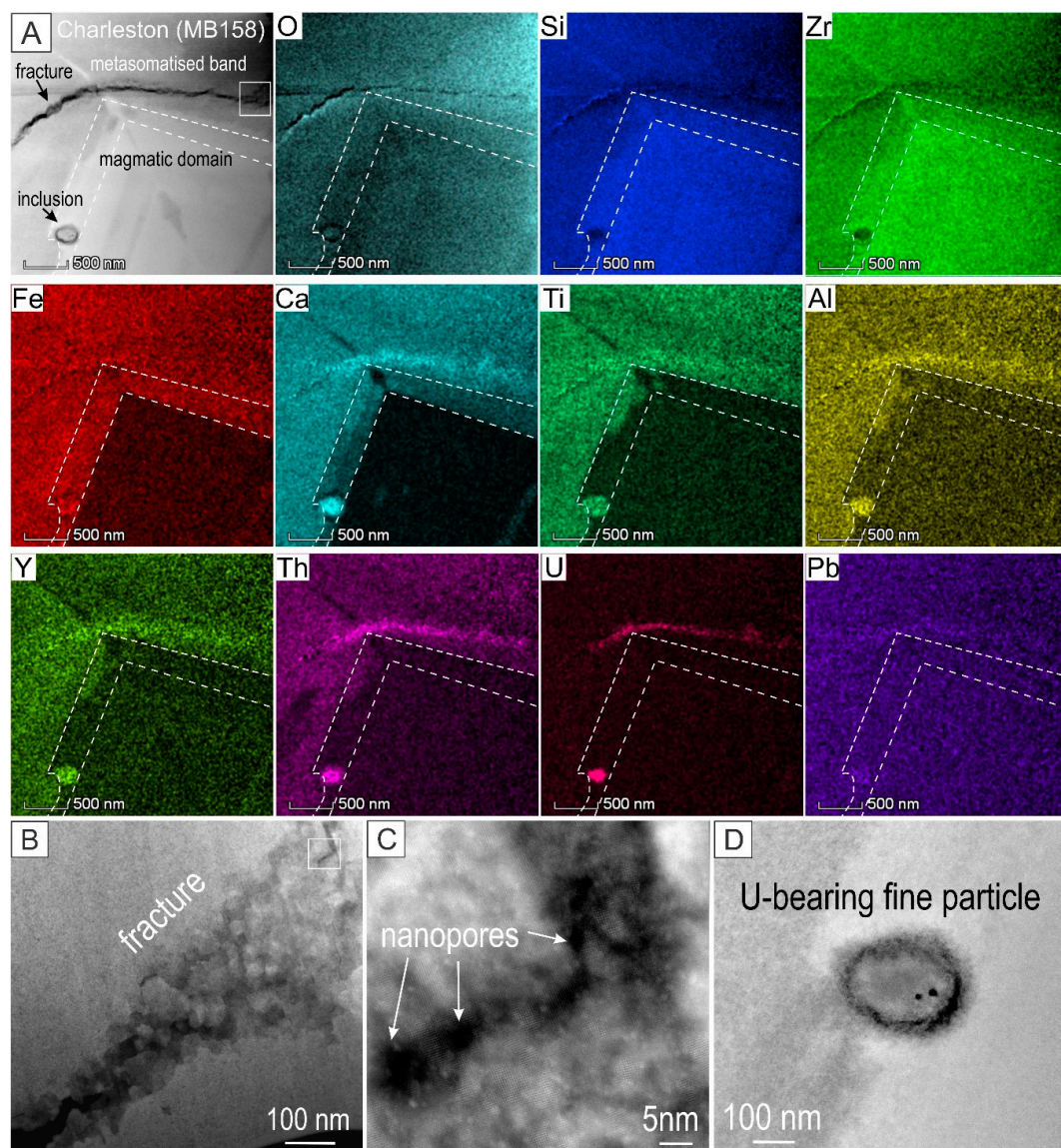


Figure 7. (A) HAADF STEM image and EDS STEM element maps of Charleston zircon (Foil #6) showing enrichment in trace elements outside of a magmatic domain as marked. Note the sharp boundary (dashed lines) for Fe but not the other elements, which instead display a diffuse boundary. Trace element (re)mobilization (all elements except Fe) along this boundary was observed along the adjacent fracture and the U-bearing fine particle. (B–D) HAADF STEM images showing zircon details along the fracture as marked. The U-bearing fine particle (D) displayed a dark rim and was beam-sensitive, indicating that it was most likely amorphous (it could not be imaged at high-resolution due to the thickness of the foil at this location). The image in (B) is the inset box indicated on (A), and image (C) shows the inset box indicated on (B). Image (D) shows detail of the inclusion from image (A).

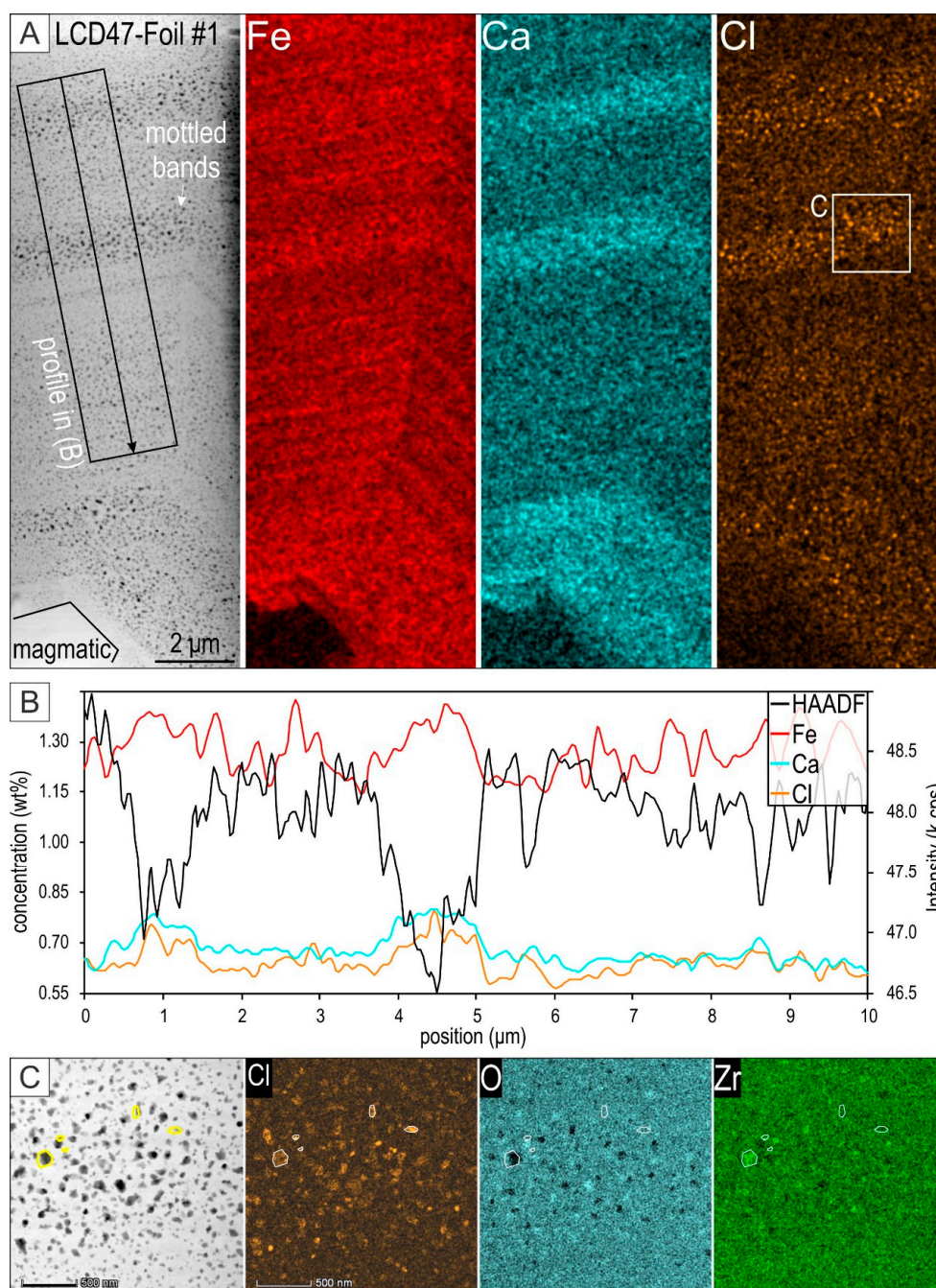


Figure 8. Trace element distributions in OD distal zircon from Foil #1. **(A)** HAADF STEM image and EDS STEM maps for Fe, Ca, and Cl showing oscillatory zoning and mottled textures. Enrichment in Ca and Cl occurred throughout the mottled bands. **(B)** Profile across the oscillatory zoning displayed positive correlation between Ca and Cl across the most intensively mottled bands. Iron distributions broadly correlated with Ca and Cl across the same bands but showed small-amplitude variation reflecting the finest-scale oscillatory banding. The HAADF intensity signal showed a negative correlation with the Ca- and Cl-enriched bands. **(C)** Image and EDS STEM maps (extended maps in Supplementary Materials C, Figure S3) of a Cl-rich area as marked in (A). Note the inconsistency in correlation between Cl with O and Zr (compare the areas outlined on the figure), e.g., high Zr and low-O where Cl-enrichment is moderate, but no changes for O and Zr for nanodomains with the highest Cl content.

The highest Cl concentration was recorded from the smallest particles (10–30 nm-diameter) of grey color, (Foil #1; Figure 10B). A profile across one of the darker particles shows that Cl was concentrated

at the edge of the particle (Figure 10C). The HAADF signal intensity and O decreased across the boundary of the particle, whereas major and minor elements displayed a slight increase. These results can also be associated with variable particle thickness, their position relative to the plane of imaging, or the presence of voids/pores, particularly for the coarser and darkest domains. Comparative imaging of the same area in both HAADF and bright-field STEM modes illustrates these features (Supplementary Materials C, Figure S1). Such voids could, however, also have been produced via the plucking out of coarser particles during ion milling.

The morphology and size of the particles throughout samples with mottled textures (Foil #1–5) varies from several nm up to 100 nm (nanoparticles) to hundreds of nm (fine particles) (Figure 11A). The largest particles, with well-defined geometrical shapes, can include pores, whereas cross-cutting darker veins will show numerous defects when imaged at high resolution (see below). Energy-dispersive X-ray maps of one medium-sized particle showed strong (lower and higher) variation in O and Zr concentrations relative to host zircon; no variation in Si was recorded (Foil #1; Figure 11B). Weak enrichment in Cl and U was present whereas Ca-rich nanoparticles occurred just outside, along the edge of the mapped particle. Overall, these results suggest that the main substitution involved replacement of O by OH^- and/or Cl leading to chloro-hydroxy-zircon formation. Although substitution of $(\text{SiO}_4)^{4-}$ tetrahedra by $4(\text{OH,Cl})^-$ can also be invoked, such a relationship is not obvious from the EDS mapping.

5.6. Atomic-Scale HAADF STEM Imaging—Zircon Crystallinity and Lattice-Scale Defects

Four main zone axes in zircon were imaged throughout the seven foils (Table 1; Figure 12A–D). In each case, imaging showed the same overall orientation across zircon in any given foil, indicating that the chemically heterogeneous domains were an integral part of the same single crystal. Despite observing evidence of lattice disorder, zircon in all samples was found to be crystalline with no amorphous areas identified. This absence of amorphous domains was observed in both the brighter bands of magmatic zircon from Cape Donington, throughout the darker or mottled bands in all other samples, and in the proximity of fractures containing newly formed phases such as xenotime.

Atomic arrangements on HAADF STEM images for the four zone axes shown in Figure 12 were interpreted using crystal structure models obtained after indexing of the Fast Fourier Transform (FFT) obtained for each image and also STEM simulations (Figure 13). These show that the brightest spots represent an overlap between Zr and Si atoms on (001) and $(1\bar{1}0)$ zone axes (Figure 13A,B), whereas both Zr (brightest, with dumbbell arrangement) and Si (darker) atoms can be resolved on the (100) and $(1\bar{1}1)$ zone axes (Figure 13C,D). There was a relatively good fit between the HAADF STEM images and simulations in each case. Such image assessment of individual zone axes by HAADF STEM was necessary to identify the presence of lattice-scale defects.

Lattice-scale defects on $(1\bar{1}1)$ zone axis in zircon were observed along a veinlet crosscutting a fine particle in Foil #1 (darker color on HAADF STEM images; Figure 14A–D). One of the defects had a hexagonal shape (Figure 14D) and showed clear modifications in both size and intensity of individual atoms relative to “normal” zircon on this zone axis (Figures 12D and 13D). An intensity profile showed changes across this defect which were interpretable as substitutions of individual Zr and Si atoms along the (011) direction (Figure 14E). Signals for Zr decrease within the defect suggesting substitution by lighter cations (e.g., Ca, Al) in variable proportions. One of the Si sites in the defect showed a higher signal relatively to host zircon, whereas the other was barely visible (correlating with darkest areas on the image). Substitution within the $(\text{SiO}_4)^{4-}$ tetrahedra can be invoked in which Me^{5+} (e.g., P^{5+}) replaces Si^{4+} , necessitating charge balance via substitution of $(\text{OH,Cl})^-$ for O^{2-} .

Lattice-scale defects were imaged on all zone axes in zircon except $(1\bar{1}0)$ (Figure 15). In magmatic zircon from Cape Donington (Foil #7), lattice disorder was found in the brighter U-richer bands (Supplementary Materials B, Table S4; Figure 2F). Square-shaped defects on the $(100)_{\text{zircon}}$ zone axis appear darker and showed arrays of single Zr (and Si—although these were less well resolved on the image) columns along the c-axis, which were doubled in the b direction leading to a smaller, squarish arrangement (outlined in Figure 15A).

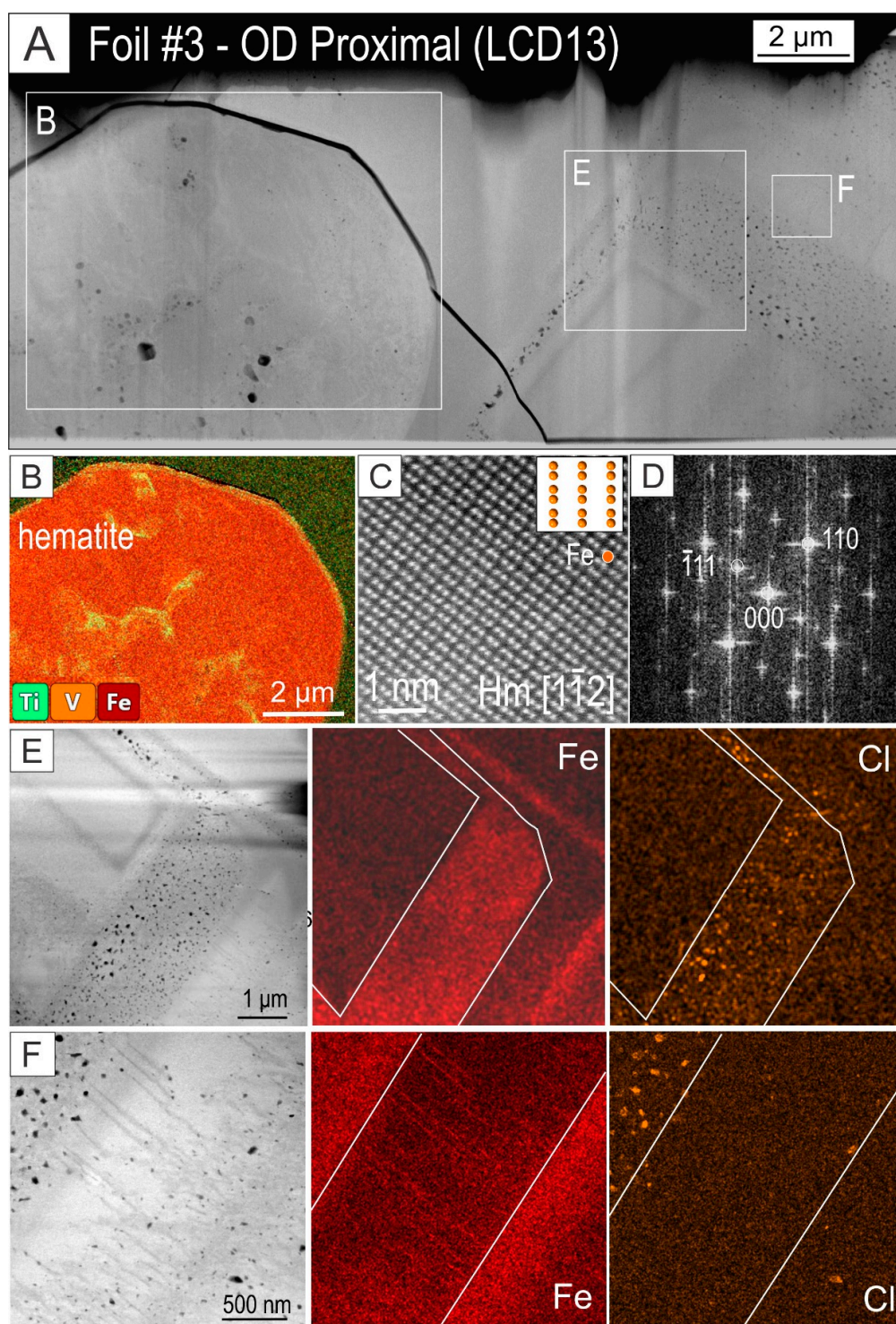


Figure 9. Trace element distributions in OD proximal zircon (Foil #3). (A) HAADF STEM image showing oscillatory banding, mottled textures, and an inclusion of hematite in zircon. High field strength element (HFSE) enrichment in hematite shown on the EDS STEM map in (B). Identification of hematite from the atomic-scale resolution image in (C) and Fast Fourier Transform (FFT) in (D) as marked. (E,F) HAADF STEM images and EDS STEM maps obtained from areas as marked on (A) (rotated 90 degrees clockwise) showing Fe and Cl enrichment throughout the mottled bands. Note the irregular distribution of Cl relative to Fe in both (E) and (F). Importantly, the Fe map in (F) shows Fe-rich veinlets crosscutting brighter bands.

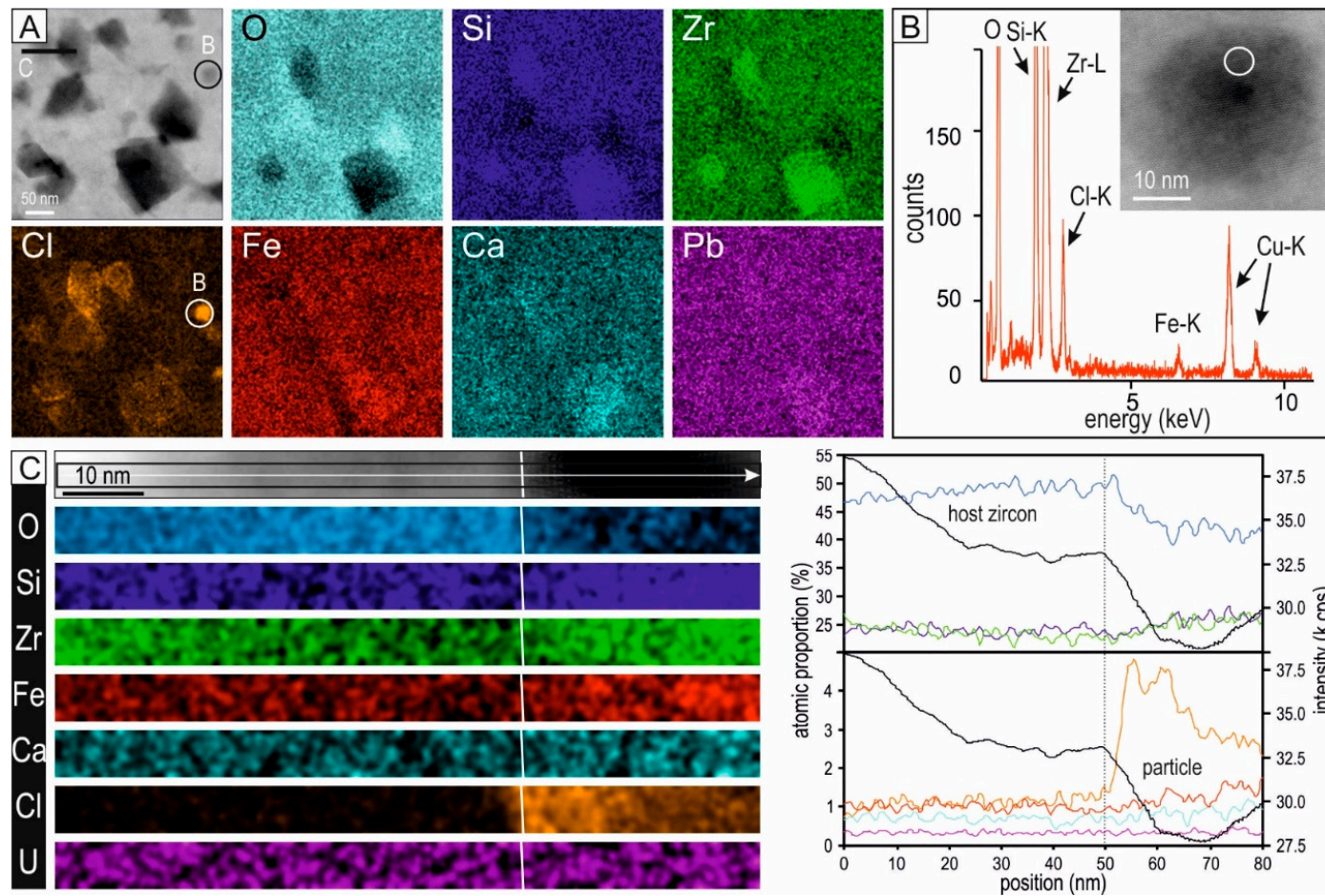


Figure 10. Aspects of nanoscale inclusions + pores throughout the mottled bands in the OD distal zircon (Foil #1). (A) Image and EDS STEM maps for a Cl-rich area selected from Figure 8C showing that the highest Cl was recorded in the smallest particles with no differences on the major or trace elements maps. Inverse correlation between O and Zr was recorded for the coarser, darkest inclusions with moderate enrichment in Cl. Note the weak variation in Fe and Ca, but not in Pb. (B) EDS spectrum for Cl-richest nanoparticle circled in (A). (C) EDS STEM maps (left) and profiles (right) across a particle with medium Cl-enrichment in (A). Profiles show high concentrations of Cl at the particle margin with increases in both major and minor elements but a strong HAADF signal decrease.

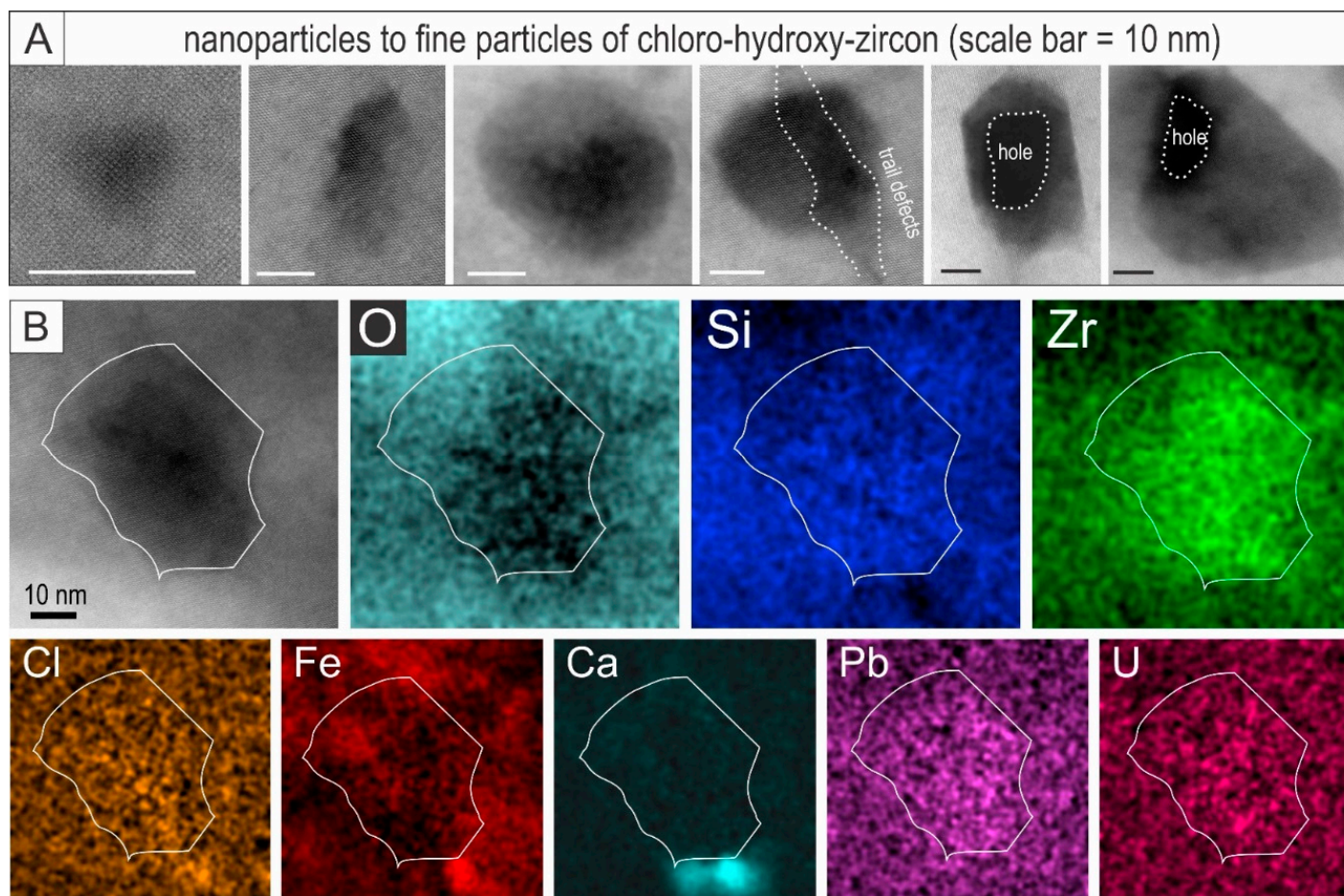


Figure 11. (A) HAADF STEM images of inclusions representative of all samples with mottled textures showing their variation in size and morphology as marked. Note the presence of rounded pores in the coarsest particles. (B) Image and EDS STEM maps of a single particle from the OD distal zircon (Foil #1). Note the strong variation in O and Zr concentration but not Si relative to host zircon and the weak relative enrichment in Cl, U, and Pb. Ca-rich nanoparticles occur just outside, at the lower edge of the mapped particle.

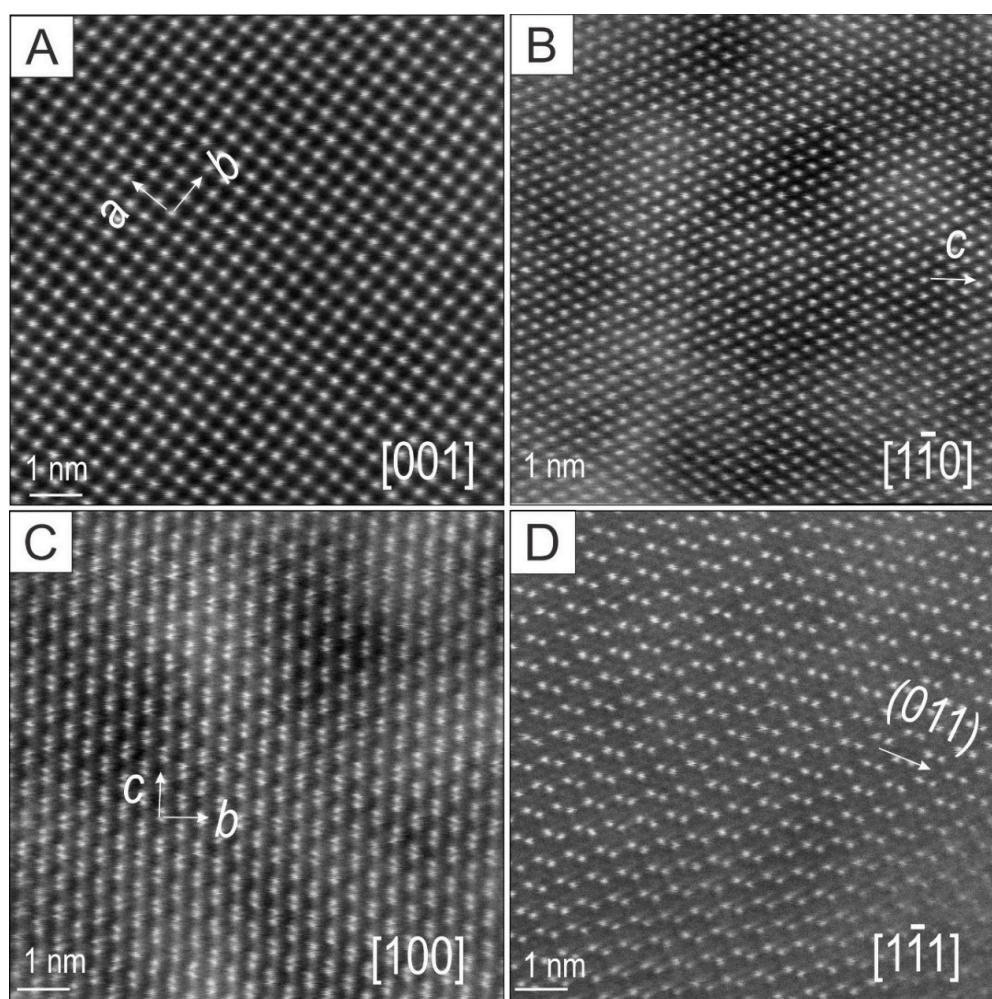


Figure 12. (A–D) High-resolution HAADF STEM images of zircon on four main zone axes as marked.

Linear defects were observed along the edge of xenotime veinlets (e.g., Wirrda Well–Donington zircon; Figure 15B). Atom displacement across the two sides of the defect can be interpreted as resulting from a simple screw dislocation considering the “atom loop” observed on the defect plane. The “loop” is illustrated by the atoms placed between the two planes with different heights relative to one another across the defect (smaller size atoms highlighted in Figure 15B). Linear defects along kink faults were imaged on (001) zone axis in Charleston zircon (Figure 15C). In this case, the fault steps/widths changed irregularly, as shown by the presence or absence of “atom loops” on the defect plane (overlays on Figure 15C). Wider planar defects, tens of nm in width, also occurred in the Charleston zircon (Figure 15D). This image can also be interpreted as a simple screw dislocation (yellow lines in Figure 15D). Interstitial atoms were inferred within the defect area only. Their size and brightness changed relative to the Zr and Si atoms on the (001) zone axis in zircon outside the defect area. Such changes could reflect differences in atom heights between the two planes on either side of the defect, or more speculatively, could be attributed to the presence of foreign atoms occurring interstitially in the zircon lattice (mixed site Ti, Ca, Th, Y, etc.). The latter supposition can be correlated with the presence of mixed sites of Ti, Ca, Th, Y, etc., as is known from zirconolite ($\text{CaZrTi}_2\text{O}_7$).

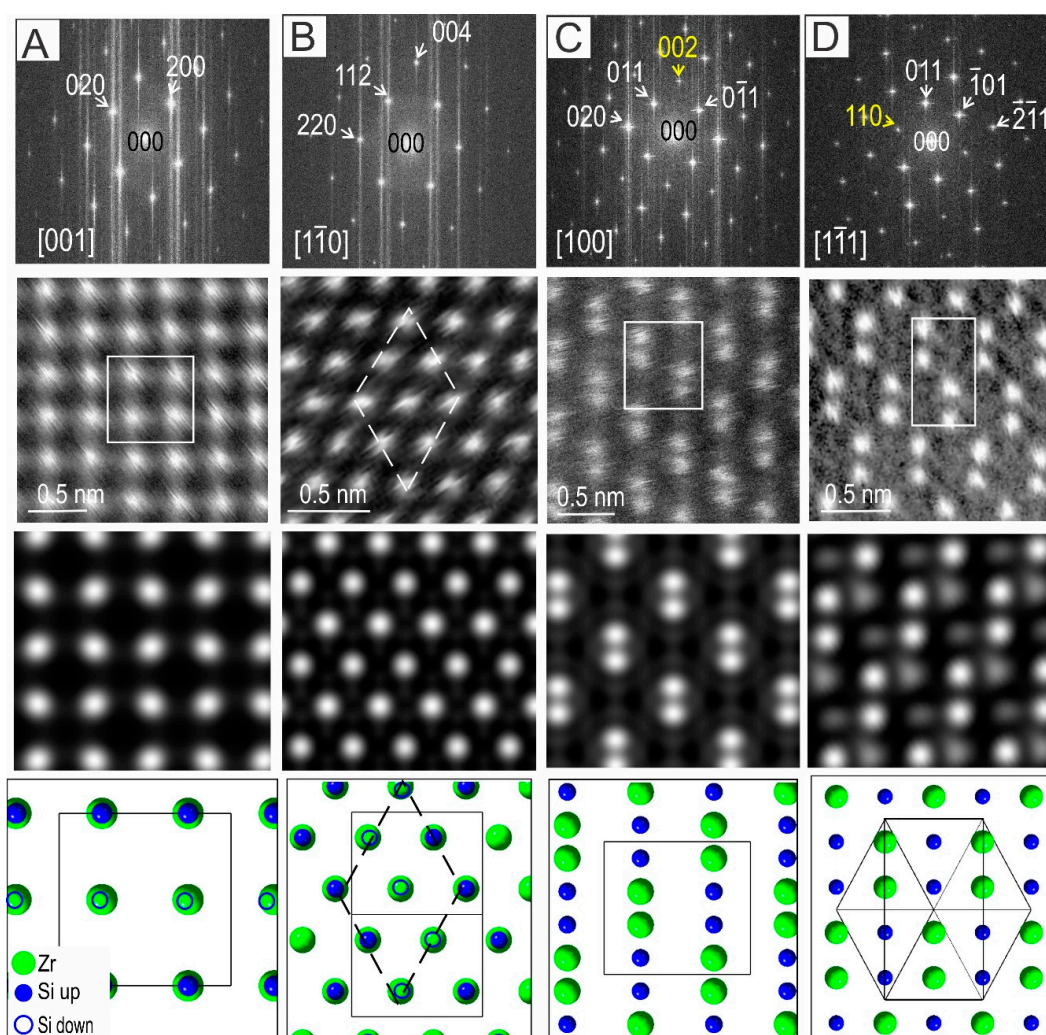


Figure 13. From top to bottom, FFT, HAADF image, STEM simulation, and crystal structure model for each of the main zone axes (A–D, as marked) imaged in zircon (Figure 12). The images and simulations were interpreted in agreement with crystal structure models on zone axes as obtained from indexing FFTs obtained from images in Figure 11. The two zone axes with dumbbell atomic arrangements (C,D) cannot be resolved using the ideal space group for zircon, $I4_1/amd$, due to the presence of forbidden reflections ($00l$; $l \neq 4n$ and $hh0$; $l \neq 4n$; marked in yellow). Indexing, crystal models, and STEM simulations were obtained using the $I2_12_12_1$ space group. The models and simulations did not change when using the $I4_1/amd$ space group.

The most complex defects were imaged in Fe-rich bands from OD distal zircon in the $[1\bar{1}1]$ zone axis (Foil #1; Figure 15E). In this case, changes in the atomic arrangement along the (011) can be interpreted as displacements with anti-phase modulation along fault planes (yellow lines in Figure 15E). In contrast, the defect within the fine particle described above (Figures 14D and 15F) can be interpreted as the result of local fluid–mineral interaction leading to an increase in OH/halogen content in the nanoparticles/fine particles.

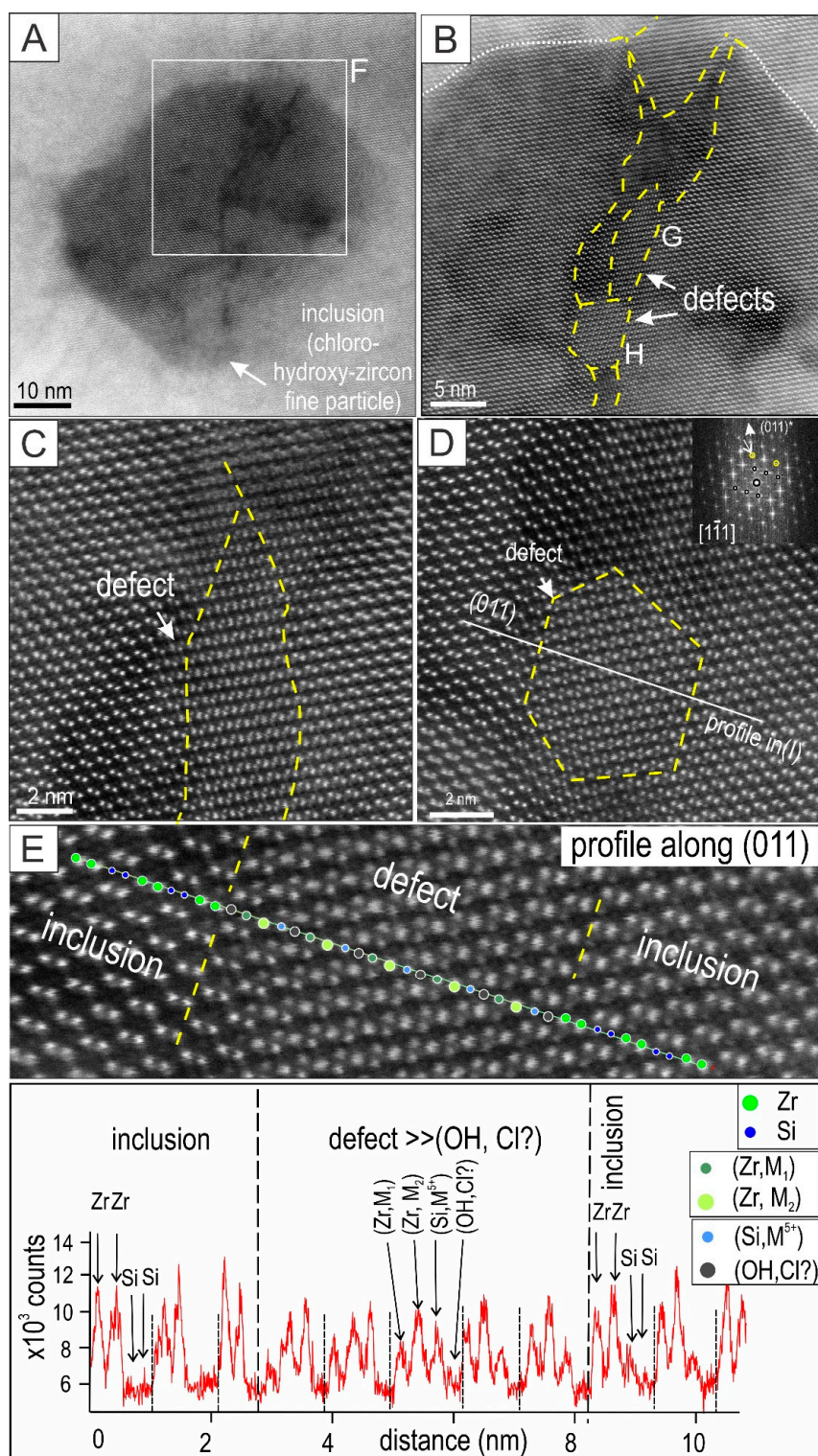


Figure 14. (A–D) Images showing defects along a fracture crosscutting one of the fine particles (Foil #1). The FFT pattern obtained from the image (inset D) shows a square sub-pattern with weaker reflections superimposed onto the main reflections. Yellow, dashed lines mark the defect shape. (E) Intensity profile across the defect in (D) showing modifications in the Zr and Si signals as marked.

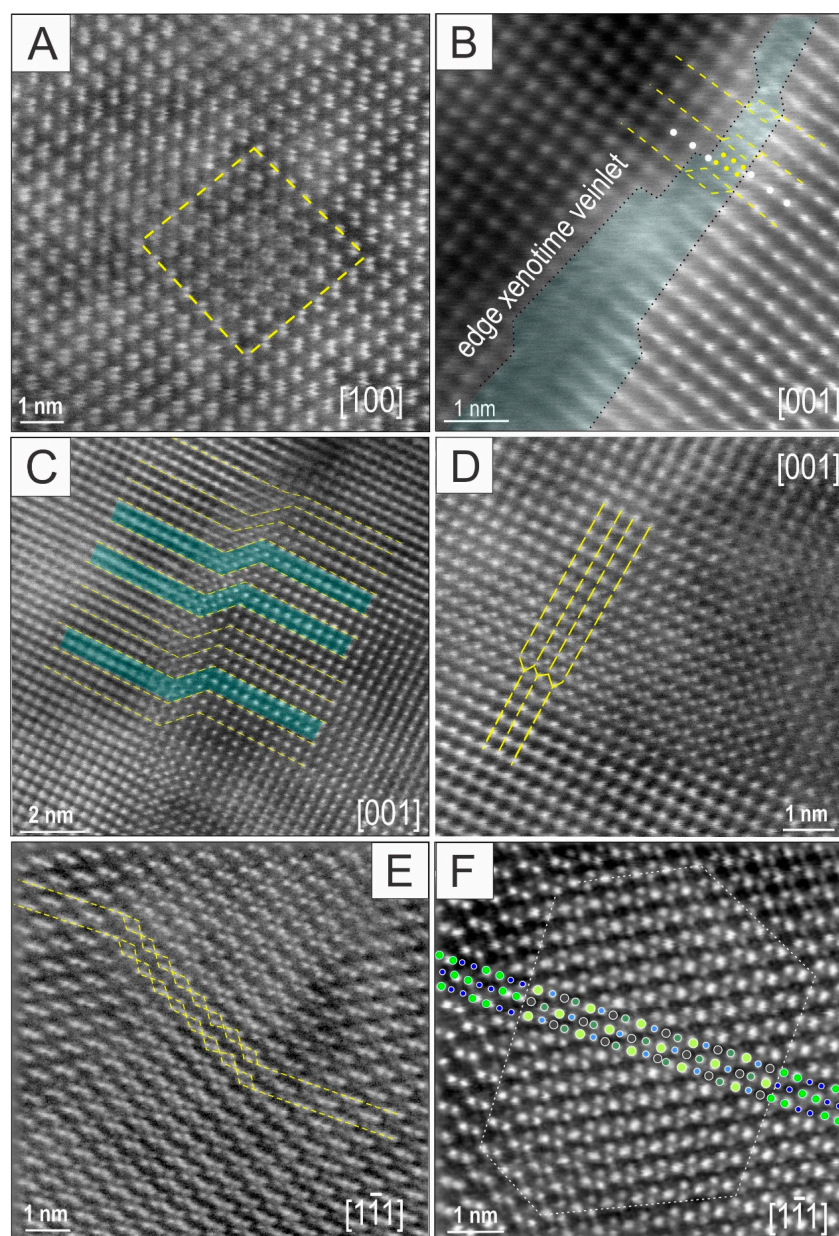


Figure 15. Atomic-scale resolution HAADF STEM images of defects in zircon. (A) Square-shaped defect (yellow outline) in U-rich bands from Cape Donington (Foil #7), tilted on the (100) zone axis. The doubling of Zr atoms observed along the *c*-axis suggests atom “stretching” along *b* induced by strain, attributable to α -recoil damage during U-decay. (B) Simple linear defect in Wirrda Well–Donington zircon (Foil #4) observed at the edge of a xenotime veinlet (blue overlay); sample tilted on the (001) zone axis in zircon. Screw dislocations (dashed lines) are marked by atom loops in the defect plane (yellow dots) relative to Zr atoms (white dots) outside the defect. (C–D) Screw dislocations (dashed lines) along a fault or at the edge of a planar defect on the (001) zone axis in Charleston zircon (Foil #6). Note irregular atom loops along the fault plane (blue overlays). (E–F) Defects in the Fe-rich, mottled bands from OD distal zircon (Foil #1) with sample tilted on the $[1\bar{1}1]$ zone axis in zircon. Antiphase atom displacement (dashed line) suggesting lattice stretching along (011) directions in (E). (F) Details of the defect (dotted line) in Figure 14D showing the size and intensity modifications in Zr and Si atoms along the (011) direction (colors as in Figure 14E). The image shows the inferred missing Si atoms as dark, regular spots along this direction.

6. Discussion

6.1. Zircon Metasomatism Down to the Nanoscale: Are Iron and Chlorine of Magmatic or Hydrothermal Origin?

It is difficult to unequivocally distinguish magmatic (primary) from secondary patterns in zircon displaying crystal oscillatory zoning with respect to Fe and Cl due to the lack of crosscutting textures and because such elements could also have been components in either granitic melts or hydrothermal fluids. For example, a magmatic origin for divalent Fe was suggested by Reference [45] based on observed substitutions. In the present study, we were able to rule out a magmatic origin by analysis of zircon from a granite belonging to the same ~1.85 Ga Donington Suite which showed the presence of Fe and Cl only in parts of the craton where they are associated with or host younger (~1.6 Ga) IOCG-type mineralization (Wirrda Well). Moreover, the concentrations of Fe and Cl in the Hiltaba Suite zircons increased with proximity to more intense mineralization. Oscillatory zoning patterns can be produced via metasomatism (ion exchange between a mineral and a percolating fluid moving through pores in a rock) in the absence of open fractures. Therefore, we stipulate that Fe–Cl zoning represents a first stage of zircon alteration via metasomatism that is quite distinct from late-stage fracture-infill or textures superimposed onto the zoning (xenotime veinlets, U-bearing nanoparticles; Figures 6–8).

Metasomatism allows partial or complete pseudomorphic replacement of one mineral by another. In some cases, the new mineral may be the same species but differs from the parent in terms of minor/trace elements, as was shown for hematite from Olympic Dam [46]. Such processes are “metasomatic” in a broader sense and occur when replacement reactions couple dissolution with (re)precipitation rates (CDRR). This interpretation concurs with empirical evidence from other studies of Hiltaba Suite granites [47], showing local alteration of magmatic feldspars or accessories via CDRR. Variation among the geochemical patterns recorded by zircon (e.g., Ca and Cl, as well as Ti, Al, Th, and Y in Charleston zircon) can be attributed to local mineralogical changes in the granite during early alkali–calcic alteration, e.g., release of cations during replacement of magmatic plagioclase by sericite or biotite by chlorite [42,47].

Metasomatism was accompanied by development of nanoscale structures, such as formation of chloro–hydroxy–zircon nanoprecipitates in all samples from the Olympic Dam district, but significantly, not in those from the Eyre Peninsula (Table 1).

Defects were observed throughout the Fe-rich bands, as well as in magmatic zircon from Cape Donington, but none show amorphization. Linear defects associated with fracture opening can be attributed to structure swelling along fission tracks (Figure 15B). This allows trace element remobilization, in turn leading to formation of U-nanoparticles or xenotime like those shown in zircon in Archean granites from Jack Hills [24,25]. Likewise, lattice expansion via stretching or screw-dislocation defects (Figure 16) can be considered part of the “swelling” induced by radiation damage.

The substitution model for metasomatized zircon shows cation exchange in which loss of 0.4–2 wt.% Si can be compensated by incorporation of OH[−] and halogens without significant removal of primary magmatic trace elements (Supplementary Materials A). Zirconium can, however, be replaced by Fe and other non-formulae cations. Chemical changes, affecting both Zr and Si, observed in defects along fractures crosscutting fine particles (Figure 14) were concordant with chloro–hydroxy–zircon of variable chemistry, as assessed by EPMA data. However, heterogeneity was observed at the nanoscale, including localized concentrations of other elements, e.g., Ca or Cl-bearing nanoparticles (Figures 10 and 11), thus explaining much of the scatter in the geochemical data obtained at the EPMA-scale.

6.2. Timing of Zircon Alteration: Is Metasomatism Pre- or Post-Metamictization?

The incorporation of Fe and associated non-formula elements relating to metasomatism as introduced above, has been extensively discussed in terms of zircon alteration linked to self-irradiation. The overarching idea is that zircon should not be able to incorporate such elements at wt.% concentration unless it accumulates radiation damage, a process resulting in swelling and amorphization, and thus, creating pathways for fluid percolation (Reference [18] and references therein).

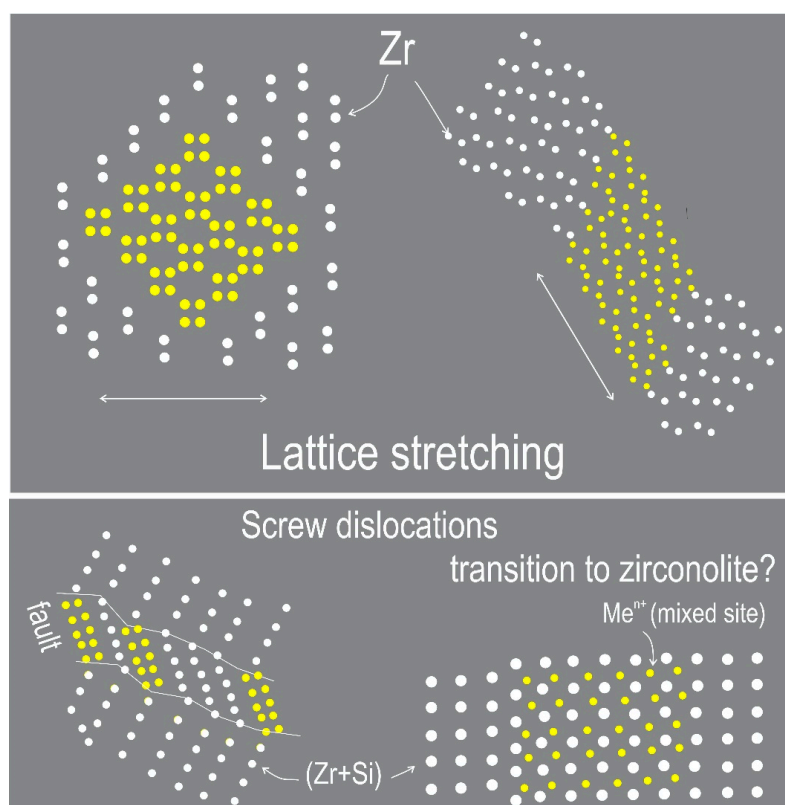


Figure 16. Schematic representation of atom arrangements in defects indicating lattice stretching and screw dislocations leading to expansion of the zircon structure. Such aspects are attributable to self-induced irradiation damage effects.

Quantification of the radiation damage necessary to facilitate major element substitution (the “First Percolation Point”) was defined as a dose of $\sim 2 \times 10^{18}$ α -decays/g (hereafter, D_c), and representing ~ 30 – 40% amorphization as a network of interconnected aperiodic domains within the crystal structure [48,49]. The link between the first percolation point and a sudden increase in non-formula elements, particularly Ca, was shown for altered zircon exhibiting U–Pb discordancy [18,19]. A high-porosity-to-spongy appearance is commonly reported, leading to deficient EPMA totals and darkening on BSE images [50]. The latter authors also contend that H_2O incorporation is promoted by pores. Nanoscale Fe- or Pb-bearing inclusions were shown in Archean zircon [24], while pores with Ca- and U-rich margins have been documented from a pegmatite zircon [26].

Using molecular dynamic simulations of alpha-recoil cascades produced via actinide decay, models of self-irradiation damage in zircon show domains of disordered material as small as a few nm [18]. However, imaging of zircon in this study (Figure 12, Figure 14, and Figure 15) did not unequivocally support this model, even for samples within the D_c range required for the crystalline-to-amorphous transition. This may relate to thermal annealing following metasomatism, e.g., associated with emplacement of the Gairdner dyke swarm at ~ 820 Ma, the most recent major tectono-thermal event recognized throughout the Gawler Craton [51].

Nevertheless, the D_c accumulation since ~ 820 Ma should have produced recognizable disorder at the nanoscale. The range of defects discussed here (Figures 14–16) are the closest expression of lattice disorder, although not truly amorphization. The positive correlation reported in other studies between high non-formula elements and D_c (e.g., [19]) is not as well-defined in this dataset. Sigmoidal trendlines shown in previous studies are comparable to that shown here, although there is a large spread in the data here, with points displaying high D_c and low Fe, and vice versa (Figure 17A). Therefore, the correlation between increasing non-formula elements and D_c may not necessarily be the result of high-U zircon creating their own pathways for increased fluid interaction. Furthermore,

high-U zircon from this study indicate the D_c required to reach the first percolation point would not have been met until ~100 Ma after zircon crystallization. This postdates the measured timing of hematite crystallization, itself a result of Fe-metasomatism [13]. The presence of hematite inclusions with an HFSE signature within Olympic Dam zircon, is further evidence of Fe–Cl-metasomatism impacting on zircon (Figure 9B) occurring in the early, magmatic-to-hydrothermal transition stage [52], rather than post-metamictization. As highlighted by trace element analysis (Figure 4; Supplementary Materials Table S4), Donington Suite data plots at lower D_c and Fe_2O_3 values than Hiltaba Suite zircon (Figure 17A) reflect the lower U-contents and lesser alteration of zircon. Even in the case of zircon in Donington Suite granite from Wirrda Well, superimposed Fe–Cl-metasomatism is recognized due to the presence of adjacent Hiltaba Suite granites linked to the same batholith that generated the RDG, host to mineralization at Olympic Dam.

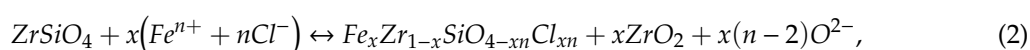
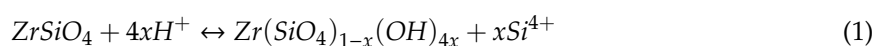
The D_c can affect U–Pb systematics in zircon and be manifest as discordance of data points via Pb loss (Figure 3). Accurate (CA)-ID-TIMS ages for magmatic crystallization can, nevertheless, be obtained [14], despite the presence of micron- to nanoscale domains, which in the present dataset do not appear to concentrate remobilized U or Pb. Such phenomena have been shown in previous studies [24,27], where they relate to alteration associated with highly metamict zircons.

6.3. Zircon Alteration Model and Magma “Fertility”

Concentrations of Cl within zircon containing Fe and other non-formula elements was measured and imaged for the first time in natural zircon. Electron microprobe maps show consistent distributions of Cl correlating with Fe in micron-scale banding (Figure 5). At the nanoscale, however, Cl was present as nanoparticles within Fe–Ca-metasomatized mottled bands (Figures 8–11). Such an association between Fe and Cl would be expected in early IOCG fluids exsolved after granite crystallization [52]. Cl-rich nanoparticles became volumetrically more significant in samples from the vicinity of the Olympic Dam deposit, while smaller amounts of Cl were also measured in the nearby Wirrda Well Donington zircon as well as Charleston zircon. In contrast, the Cape Donington zircon displayed a complete absence of Cl. Therefore, we concluded that Cl was inherent to hydrothermal fluids derived from the Hiltaba Suite granites. Moreover, such Fe–Cl-bearing fluids also affected nearby older granites (Donington Suite), host to ~1.6 Ga IOCG mineralization at Wirrda Well.

Zircon metasomatism can be attributed to a low-fluid, mineral-buffered diffusion-reaction process in the beginning (only crystal zoning), followed by formation of chloro–hydroxy–zircon nanoprecipitates when fluids become highly focused (Figure 17B). Iron-rich nano-veinlets begin to interconnect across crystal zones previously metasomatized during increase in the flux of Fe-rich fluids (formation of hematite inclusions; Figure 9). Comparable phenomena in which a mineral can host nanoscale inclusions of the same mineral but with subtle yet distinct chemical differences, are known from Fe oxides, notably Si–Fe nanoprecipitates within silician magnetite. These are documented both from banded iron formation deposits [53] and the Olympic Dam deposit [54].

The preservation of pre-existing crystal orientation in zircon nanoprecipitates and host zircon is characteristic of reactions via a sharp interface, typical of CDRR replacement. Moreover, transient porosity developed during CDRR progression provides sites for deposition of nanoprecipitates, as suggested here and elsewhere (e.g., [55–57]). Hydrothermal fluids interacting with zircon can be considered acidic based on the hydrated-substitution model for zircon (Supplementary Materials A and B, Table S4). Fluid transport of Fe, from the granite-derived fluid and Ca + Al from breakdown of minerals in the granite via alkali–calcic alteration is likely to occur as chloride complexes and can lead to Si and/or Zr loss, according to the reactions:



where $n = 2$ or 3 , and $x = 0$ to 1 .

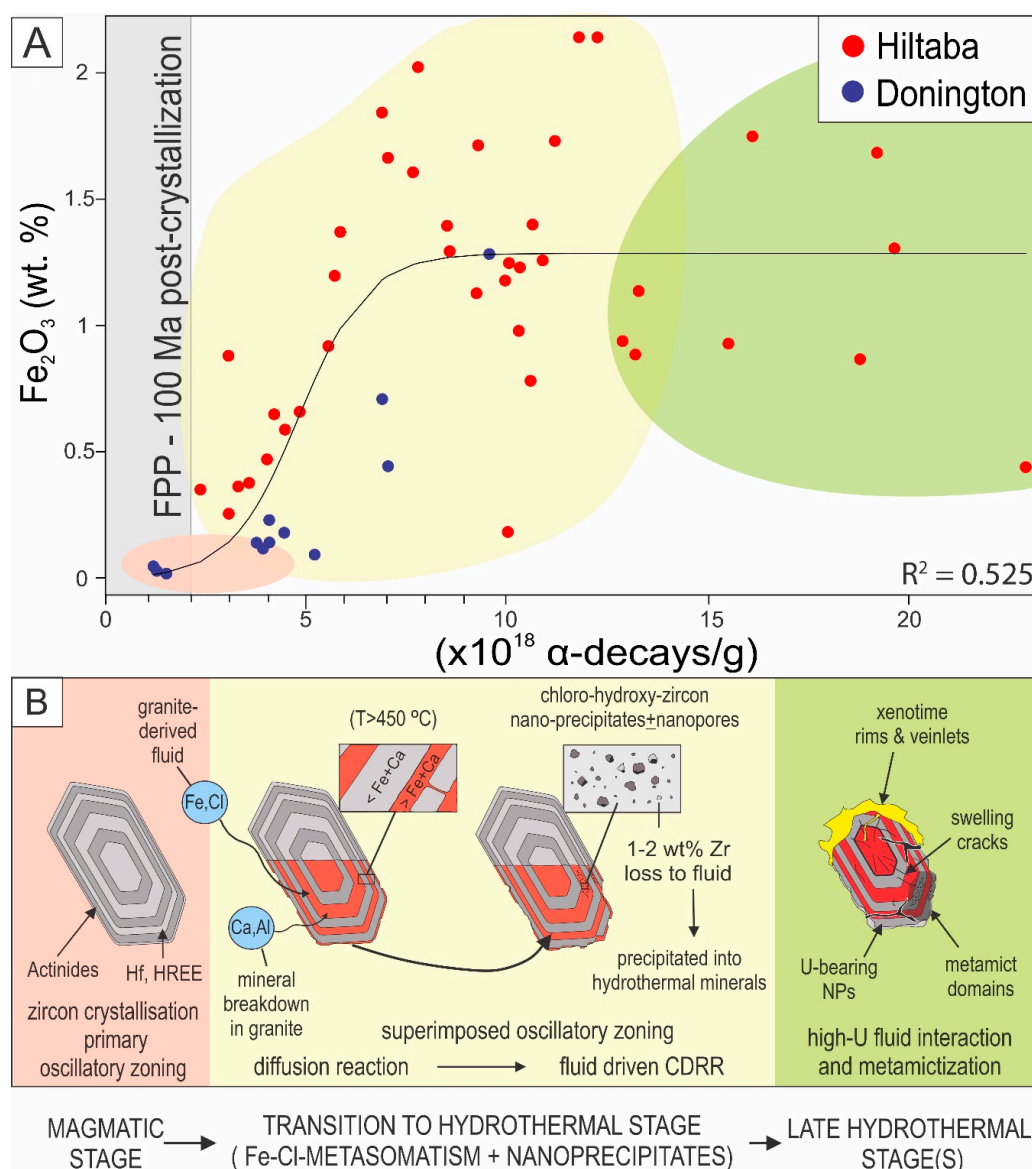


Figure 17. (A) Plot of Fe₂O₃ (wt.%) versus D_c ($\times 10^{18}$ α -decays/g) for all zircon samples as marked and using EPMA data from Supplementary Materials B, Table S4 (four analyses with $D_c > 25$ were excluded). A sigmoid through the data was fit by non-linear least squares regression using the software “R”. Although the first percolation point (FPP) for zircon was marked at $D_c = 2$ (as defined by Salje et al. [48]), a sharp increase in wt.% Fe₂O₃ was seen only at $D_c = \sim 3$. The FPP in Olympic Dam zircon was only reached at least 100 Ma after crystallization, using the dose concentration calculation of Meldrum et al. [58]. Also, note the scatter in the dataset concordant with the weak correlation between the highest measured non-formula element (Fe) and D_c . (B) Schematic diagram illustrating evolution of magmatic zircon from granites in the Olympic Cu–Au Province. Colored areas in (A) correspond to the main evolutionary stages in (B). Note that Cape Donington zircon, with the lowest non-formula elements, plots in a magmatic domain that straddles the FPP line. In contrast, analyses with high U concentration corresponded to intensively altered stages (green), featuring superimposed textures with all the characteristic of metamict zircon, possibly resulting from interaction with late-stage, U-rich hydrothermal fluids. Metasomatic textures and association with abundant, Cl-rich nanoprecipitates are typical features of fertile granites. The association between Fe and Cl recorded in metasomatized zircon during magmatic-to-hydrothermal transition is a diagnostic signature of fertile IOCG systems.

The Fe–Cl-rich signature of post-magmatic fluids is recorded within the mottled textures of zircon and represents the onset of IOCG mineralization during the magmatic-to-hydrothermal transition. From ID-TIMS dating of hematite, iron metasomatism is known to have occurred at Olympic Dam shortly after granite crystallization (~2–4 Ma later) [13]. The present data support early, as well as prolonged, zircon alteration, illustrated here from areas that are overprinting primary growth (Figure 2B,D). The Fe–Cl-rich metasomatized zones within zircon were also imaged directly adjacent to magmatic relict domains (Figure 8A). Recrystallization of zircon surrounding xenotime veinlets was observed down to the nanoscale (Supplementary Materials C, Figure S3). Whereas zircon metasomatism overprinting primary growth zoning can be related to the earliest hydrothermal fluids exsolved at the depth of granite emplacement, later cycles of zircon alteration could happen during and/or after granite uplift as the IOCG mineralizing system evolved.

Overall, the increase in Cl associated with abundant chloro–hydroxy–zircon nanoprecipitates correlates with proximity to the Olympic Dam orebody. Such features can, thus, be considered a direct indicator of magma “fertility” (the ability of a magma to generate hydrothermal fluids that are sufficiently well-endowed with Cu, U, etc., to form a sizable ore deposit) in Hiltaba Suite granites. Furthermore, the presence of Cl in zircon from other Hiltaba Suite granites such as Charleston, indicates potential undiscovered IOCG mineralization using the zircon pathfinder.

7. Conclusions and Implications

1. From the case studies presented and comparison between them, zircon may be substituted with non-formula elements, notably Fe and Cl, released ~2–4 Ma after magmatic crystallization, during a widespread metasomatic event, prior to fluid pathway development during metamictization.

2. Chloro–hydroxy–zircon nanoprecipitates record the Fe–Cl-signature of fluids released during the magmatic-to-hydrothermal transition in IOCG systems, which volumetrically increase in granites of different age with proximity to Olympic Dam. Such nanoprecipitates represent a potential pathfinder to mineralization associated with fertile granites. Although we recommend that the data should initially be tested in other IOCG terranes, there exists potential for similar features to be identified within zircon from other deposit types involving penetrative metasomatic alteration.

3. Relationships between micron- and nanoscale observations in zircon are a largely untapped research field. With ever increasing instrumental resolution and analytical precision, nanoscale studies can provide new insights into processes carrying implications for geochronology, ore deposit genesis and mineral exploration.

4. In summary, this study has shown that early metasomatic alteration can be recorded in magmatic zircon and that these patterns can be preserved over geological time, even when superimposed by the effects of metamictization. This implies that nanoscale studies of magmatic zircon, when coupled with careful micron-scale characterization of textures and compositions, could represent a valuable new tool in mineral exploration.

Supplementary Materials: The following are available online at <http://www.mdpi.com/2075-163X/9/6/364/s1>, Supplementary Materials A: Extended details of methodology (Tables S1 and S2); Supplementary Materials B: Expanded data tables (Tables S3–S5); Supplementary Materials C: Additional figures (Figures S1, S2, and S3A–S3E).

Author Contributions: L.C.-D. and C.L.C. conceived this contribution. Analytical work was conducted L.C.-D., C.L.C., M.R.V.-I., M.D., W.K., J.X. and U.I.D., with A.S. operating the Titan Themis instrument and B.P.W. assisting with EPMA set-up. The manuscript was written by L.C.-D., C.L.C., M.R.V.-I. and N.J.C., with contributions from K.E., A.K.-C. and B.P.W.

Funding: This research was funded from the project “Trace elements in iron-oxides: deportment, distribution and application in ore genesis, geochronology, exploration and mineral processing”, supported by BHP Olympic Dam and the South Australian Government Mining and Petroleum Services Centre of Excellence. N.J.C. and K.E. acknowledge funding from the ARC Research Hub for Australian Copper–Uranium (Grant IH130200033).

Acknowledgments: We acknowledge the AMMRF for instrument access. Sarah Gilbert assisted with LA-ICP-MS analysis and Animesh Basak assisted with FIB-SEM operation. Chris Kalnins is thanked for preparing two of the TEM foils presented. We kindly thank two anonymous reviewers for comments that helped improve this manuscript.

Conflicts of Interest: The authors declare no conflicts of interest.

References

1. Groves, D.I.; Bierlein, F.P.; Meinert, L.D.; Hitzman, M.W. Iron oxide copper-gold (IOCG) deposits through Earth history: Implications for origin, lithospheric setting, and distinction from other epigenetic iron oxide deposits. *Econ. Geol.* **2010**, *105*, 641–654. [[CrossRef](#)]
2. Barton, M.D. Iron oxide (–Cu–Au–REE–P–Ag–U–Co) systems. In *Treatise on Geochemistry*, 2nd ed.; Elsevier: Amsterdam, The Netherlands, 2014; Volume 13, pp. 515–541.
3. Krneta, S.; Ciobanu, C.L.; Cook, N.J.; Ehrig, K.; Kontonikas-Charos, A. Apatite at Olympic Dam, South Australia: A petrogenetic tool. *Lithos* **2016**, *262*, 470–485. [[CrossRef](#)]
4. Krneta, S.; Ciobanu, C.L.; Cook, N.J.; Ehrig, K.J. Numerical modeling of REE fractionation patterns in fluorapatite from the Olympic Dam deposit (South Australia). *Minerals* **2018**, *8*, 342. [[CrossRef](#)]
5. Condon, D.J.; Schmitz, M.D. One hundred years of geochronology. *Elements* **2013**, *9*, 3–80. [[CrossRef](#)]
6. Harley, S.L.; Kelly, N.M. Zircon Tiny but Timely. *Elements* **2007**, *3*, 13–18. [[CrossRef](#)]
7. Rubatto, D.; Hermann, J. Zircon behaviour in deeply subducted rocks. *Elements* **2007**, *3*, 31–35. [[CrossRef](#)]
8. Scherer, E.E.; Whitehouse, M.J.; Munker, C. Zircon as a Monitor of Crustal Growth. *Elements* **2007**, *3*, 19–24. [[CrossRef](#)]
9. Hoskin, P.W.O.; Schaltegger, U. The composition of zircon and igneous and metamorphic petrogenesis. *Rev. Mineral. Geochem.* **2003**, *53*, 27–62. [[CrossRef](#)]
10. Ewing, R.C.; Meldrum, A.; Wang, L.M.; Weber, W.J.; Corrales, L.R. Radiation damage in zircon. *Rev. Mineral. Geochem.* **2003**, *53*, 387–425. [[CrossRef](#)]
11. Skirrow, R.G.; Bastrakov, E.N.; Barovich, K.; Fraser, G.L.; Creaser, R.A.; Fanning, C.M. Timing of iron oxide Cu–Au–(U) hydrothermal activity and Nd isotope constraints on metal sources in the Gawler craton, South Australia. *Econ. Geol.* **2007**, *102*, 1441–1470. [[CrossRef](#)]
12. Ehrig, K.; McPhie, J.; Kamenetsky, V. Geology and Mineralogical Zonation of the Olympic Dam Iron Oxide Cu–U–Au–Ag Deposit, South Australia. In *Geology and Genesis of Major Copper Deposits and Districts of the World: A Tribute to Richard H. Sillitoe*; Hedenquist, J.W., Harris, M., Camus, F., Eds.; Society of Economic Geologists Special Publication 16; Society of Economic Geologists: Littleton, CO, USA, 2012; pp. 237–267.
13. Courtney-Davies, L.; Tapster, S.; Ciobanu, C.; Cook, N.J.; Verdugo-Ihl, M.R.; Ehrig, K.J.; Kennedy, A.K.; Gilbert, S.E.; Condon, D.J.; Wade, B.P. A multi-technique evaluation of hydrothermal hematite U–Pb isotope systematics: Implications for ore deposit geochronology. *Chem. Geol.* **2019**, *513*, 54–72. [[CrossRef](#)]
14. Cherry, A.R.; Ehrig, K.; Kamenetsky, V.S.; McPhie, J.; Crowley, J.L.; Kamenetsky, M.B. Precise geochronological constraints on the origin, setting and incorporation of ca. 1.59 Ga surficial facies into the Olympic Dam Breccia Complex, South Australia. *Precamb. Res.* **2018**, *315*, 162–178. [[CrossRef](#)]
15. Ewing, R.C.; Lutze, W.; Weber, W.J. Zircon—A Host-Phase for the Disposal of Weapons Plutonium. *J. Mater. Res.* **1995**, *10*, 243–246. [[CrossRef](#)]
16. Holland, H.D.; Gottfried, D. The effect of nuclear radiation on the structure of zircon. *Acta Cryst.* **1955**, *8*, 291–300. [[CrossRef](#)]
17. Mattinson, J. Zircon U–Pb chemical abrasion (“CA–TIMS”) method: Combined annealing and multi-step partial dissolution analysis for improved precision and accuracy of zircon ages. *Chem. Geol.* **2005**, *220*, 47–66. [[CrossRef](#)]
18. Geisler, T.; Schaltegger, U.; Tomaschek, F. Re-equilibration of zircon in aqueous fluids and melts. *Elements* **2007**, *3*, 43–50. [[CrossRef](#)]
19. Geisler, T.; Rashwan, A.A.; Rahn, M.K.W.; Poller, U.; Zwingmann, H.; Pidgeon, R.T.; Schleicher, H.; Tomaschek, F. Low temperature hydrothermal alteration of natural metamict zircons from the Eastern Desert, Egypt. *Mineral. Mag.* **2003**, *67*, 485–508. [[CrossRef](#)]
20. Tang, F.; Taylor, J.M.; Einsle, J.F.; Borlina, C.S.; Fu, R.R.; Weiss, B.P.; Williams, H.M.; Williams, W.; Nagy, L.; Midgley, P.; et al. Secondary magnetite in ancient zircon precludes analysis of a Hadean geodynamo. *Proc. Natl. Acad. Sci. USA* **2019**, *116*, 407–412. [[CrossRef](#)]
21. Lu, Y.J.; Loucks, R.R.; Fiorentini, M.L.; McCuaig, T.C.; Evans, N.J.; Yang, Z.M.; Hou, Z.Q.; Kirkland, C.L.; Parra-Avila, L.A.; Kobussen, A. Zircon compositions as a pathfinder for porphyry Cu ± Mo ± Au deposits. *Econ. Geol.* **2016**, *19*, 329–347.

22. Belousova, E.A.; Griffin, W.L.; O'Reilly, S.Y.; Fisher, N.I. Igneous zircon: Trace element composition as an indicator of source rock type. *Contrib. Mineral. Petrol.* **2002**, *143*, 602–622. [[CrossRef](#)]
23. Utsunomiya, S.; Ewing, R.C. Application of high-angle annular dark field scanning transmission electron microscopy—Energy dispersive X-ray spectrometry, and energy-filtered transmission electron microscopy to the characterization of nanoparticles in the environment. *Environ. Sci. Technol.* **2003**, *37*, 786–791. [[CrossRef](#)]
24. Utsunomiya, S.; Palenik, C.S.; Valley, J.W.; Cavosie, A.J.; Wilde, S.A.; Ewing, R.C. Nanoscale occurrence of Pb in an Archean zircon. *Geochim. Cosmochim. Acta* **2004**, *68*, 4679–4686. [[CrossRef](#)]
25. Utsunomiya, S.; Valley, J.W.; Cavosie, A.J.; Wilde, S.A.; Ewing, R.C. Radiation damage and alteration of zircon from a 3.3 Ga porphyritic granite from the Jack Hills, Western Australia. *Chem. Geol.* **2007**, *236*, 92–111. [[CrossRef](#)]
26. Seydoux-Guillaume, A.M.; Bingen, B.; Paquette, J.L.; Bosse, V. Nanoscale evidence for uranium mobility in zircon and the discordance of U-Pb chronometers. *Earth Plan. Sci. Lett.* **2015**, *409*, 43–48. [[CrossRef](#)]
27. Kusiak, M.A.; Dunkley, D.J.; Wirth, R.; Whitehouse, M.J.; Wilde, S.A.; Marquardt, K. Metallic lead nanospheres discovered in ancient zircons. *Proc. Natl. Acad. Sci. USA* **2015**, *112*, 4958–4963. [[CrossRef](#)]
28. Ciobanu, C.L.; Cook, N.J.; Maunders, C.; Wade, B.P.; Ehrig, K. Focused Ion Beam and Advanced Electron Microscopy for Minerals: Insights and Outlook from Bismuth Sulphosalts. *Minerals* **2016**, *6*, 112. [[CrossRef](#)]
29. Cook, N.J.; Ciobanu, C.L.; Ehrig, K.; Slattey, A.; Verdugo-Ihl, M.R.; Courtney-Davies, L.; Gao, W. Advances and opportunities in ore mineralogy. *Minerals* **2017**, *7*, 233. [[CrossRef](#)]
30. Goldfarb, R.J.; Bradley, D.; Leach, D.L. Secular variation in economic geology. *Econ. Geol.* **2010**, *105*, 459–465. [[CrossRef](#)]
31. Allen, S.R.; McPhie, J.; Ferris, G.; Simpson, C. Evolution and architecture of a large felsic igneous province in western Laurentia: The 1.6 Ga Gawler Range Volcanics, South Australia. *J. Volcanol. Geotherm. Res.* **2008**, *172*, 132–147. [[CrossRef](#)]
32. Keyser, W.M.; Ciobanu, C.L.; Cook, N.J.; Johnson, G.; Feltus, F.; Johnson, S.; Dmitrijeva, M.; Ehrig, K.; Nguyen, P. Petrography and trace element signatures of iron-oxides in deposits from the Middleback Ranges, South Australia: From banded iron formation to ore. *Ore Geol. Rev.* **2018**, *93*, 337–360. [[CrossRef](#)]
33. Domnick, U.; Cook, N.J.; Bluck, R.; Brown, C.; Ciobanu, C.L. Petrography of granitoids from the Samphire Pluton, South Australia: Implications for uranium mineralization in overlying sediments. *Lithos* **2018**, *300–301*, 1–19. [[CrossRef](#)]
34. Keyser, W.; Ciobanu, C.L.; Cook, N.J.; Dmitrijeva, M.; Courtney-Davies, L.; Feltus, H.; Gilbert, S.; Johnson, G.; Ehrig, K. Iron-oxides constrain BIF evolution in terranes with protracted geological histories: The Iron Count prospect, Middleback Ranges, South Australia. *Lithos* **2019**, *324*, 20–38. [[CrossRef](#)]
35. Dmitrijeva, M.; Metcalfe, A.V.; Ciobanu, C.L.; Cook, N.J.; Frenzel, M.; Keyser, W.M.; Johnson, G.; Ehrig, K. Discrimination and variance structure of trace element signatures in hematite: A case study of BIF-mineralization from the Middleback Ranges, South Australia. *Math. Geosci.* **2018**, *50*, 381–415. [[CrossRef](#)]
36. Creaser, R.A.; Fanning, C.M. A U-Pb zircon study of the Mesoproterozoic Charleston Granite, Gawler Craton, South Australia. *Aust. J. Earth Sci.* **1993**, *40*, 519–526. [[CrossRef](#)]
37. Skirrow, R.G.; van der Wielen, S.E.; Champion, D.C.; Czarnota, K.; Thiel, S. Lithospheric architecture and mantle metasomatism linked to iron oxide Cu-Au ore formation: Multidisciplinary evidence from the Olympic Dam Region, South Australia. *Geochem. Geophys. Geosyst.* **2018**, *19*, 2673–2705. [[CrossRef](#)]
38. Wade, C.E.; Payne, J.L.; Barovich, K.M.; Reid, A.J. Heterogeneity of the sub-continental lithospheric mantle and 'non-juvenile' mantle additions to a Proterozoic silicic large igneous province. *Lithos* **2019**, *340–341*, 87–107. [[CrossRef](#)]
39. Ovalle, J.T.; La Cruz, N.L.; Reich, M.; Barra, F.; Simon, A.C.; Konecke, B.A.; Rodriguez-Mustafa, M.A.; Deditius, A.P.; Childress, T.M.; Morata, D. Formation of massive iron deposits linked to explosive volcanic eruptions. *Sci. Rep.* **2018**, *8*, 14855. [[CrossRef](#)]
40. Kontonikas-Charos, A.; Ciobanu, C.L.; Cook, N.J.; Ehrig, K.; Krneta, S.; Kamenetsky, V.S. Feldspar evolution in the Roxby Downs Granite, host to Fe-oxide Cu-Au-(U) mineralisation at Olympic Dam, South Australia. *Ore Geol. Rev.* **2017**, *80*, 838–859. [[CrossRef](#)]
41. Krneta, S.; Cook, N.J.; Ciobanu, C.L.; Ehrig, K.; Kontonikas-Charos, A. The Wirrda Well and Acropolis prospects Gawler Craton, South Australia: Insights into evolving fluid conditions through apatite chemistry. *J. Geochem. Explor.* **2017**, *181*, 276–291. [[CrossRef](#)]

42. Kontonikas-Charos, A.; Ciobanu, C.L.; Cook, N.J.; Ehrig, K.; Krneta, S.; Kamenetsky, V.S. Rare earth element geochemistry of feldspars: Examples from Fe-oxide Cu-Au systems in the Olympic Cu-Au Province, South Australia. *Mineral. Petrol.* **2018**, *112*, 145–172. [[CrossRef](#)]
43. Jagodzinski, E.A. Compilation of SHRIMP U-Pb geochronological data Olympic Domain, Gawler Craton, South Australia, 2001–2003. *Geosci. Aust. Rec.* **2005**, *20*, 2005.
44. Keyser, W.; Ciobanu, C.L.; Cook, N.J.; Courtney-Davies, L.; Kennedy, A.; Wade, B.P.; Ehrig, K.; Dmitrijeva, M.; Kontonikas-Charos, A.; Feltus, H.; et al. Petrographic and geochronological constraints on the granitic basement to the Middleback Ranges, South Australia. *Precamb. Res.* **2019**, *324*, 170–193. [[CrossRef](#)]
45. Pérez-Soba, C.; Villaseca, C.; González del Tánago, J.; Nasdala, L. The composition of zircon in the peraluminous Hercynian granites of the Spanish Central System batholith. *Can. Mineral.* **2007**, *45*, 509–527. [[CrossRef](#)]
46. Verdugo-Ihl, M.R.; Ciobanu, C.L.; Cook, N.J.; Ehrig, K.; Courtney-Davies, L.; Gilbert, S. Textures and U-W-Sn-Mo signatures in hematite from the Cu-U-Au-Ag orebody at Olympic Dam, South Australia: Defining the archetype for IOCG deposits. *Ore Geol. Rev.* **2017**, *91*, 173–195. [[CrossRef](#)]
47. Kontonikas-Charos, A.; Ciobanu, C.L.; Cook, N.J.; Ehrig, K.; Ismail, R.; Krneta, S.; Basak, A. Feldspar mineralogy and rare earth element (re)mobilization in iron-oxide copper gold systems from South Australia: A nanoscale study. *Mineral. Mag.* **2018**, *82*, S173–S197. [[CrossRef](#)]
48. Salje, E.K.H.; Chrosch, J.; Ewing, R.C. Is “metamictization” of zircon a phase transition? *Am. Mineral.* **1999**, *84*, 1107–1116. [[CrossRef](#)]
49. Ríos, S.; Malcherek, T.; Salje, E.K.H.; Domeneghetti, C. Localized defects in radiation-damaged zircon. *Acta Cryst.* **2000**, *56*, 947–952. [[CrossRef](#)]
50. Nasdala, L.; Kronz, A.; Wirth, R.; Váczi, T.; Pérez-Soba, C.; Willner, A.; Kennedy, A.K. Alteration of radiation-damaged zircon and the related phenomenon of deficient electron microprobe totals. *Geochim. Cosmochim. Acta* **2009**, *73*, 1637–1650. [[CrossRef](#)]
51. Wingate, M.T.D.; Campbell, I.H.; Compston, W.; Gibson, G.M. Ion microprobe U–Pb ages for Neoproterozoic basaltic magmatism in south-central Australia and implications for the breakup of Rodinia. *Precamb. Res.* **1998**, *87*, 135–159. [[CrossRef](#)]
52. Verdugo-Ihl, M.R.; Ciobanu, C.L.; Cook, N.J.; Ehrig, K.; Courtney-Davies, L. Defining early stages of IOCG systems: Evidence from iron-oxides in the outer shell of the Olympic Dam deposit, South Australia. *Mineral. Depos.* **2019**. [[CrossRef](#)]
53. Xu, H.; Shen, Z.; Konishi, H. Si-magnetite nano-precipitates in silician magnetite from banded iron formation: Z-contrast imaging and ab initio study. *Am. Mineral.* **2014**, *99*, 2196–2202. [[CrossRef](#)]
54. Ciobanu, C.L.; Verdugo-Ihl, M.R.; Slattery, A.; Cook, N.J.; Ehrig, K.; Courtney-Davies, L.; Wade, B.P. Silician magnetite: Si-Fe-nanoprecipitates and other mineral inclusions in magnetite from the Olympic Dam deposit, South Australia. *Minerals* **2019**, *9*, 311. [[CrossRef](#)]
55. Tooth, B.; Ciobanu, C.L.; Green, L.; O'Neill, B.; Brugger, J. Bi-melt formation and gold scavenging from hydrothermal fluids: An experimental study. *Geochim. Cosmochim. Acta* **2011**, *75*, 5423–5443. [[CrossRef](#)]
56. Verdugo-Ihl, M.R.; Ciobanu, C.L.; Cook, N.J.; Slattery, A.; Ehrig, K. Copper nanoparticles along fluid inclusion trails in hematite. In Proceedings of the Goldschmidt 2018, Boston, MA, USA, 12–17 August 2018.
57. Owen, N.D.; Ciobanu, C.L.; Cook, N.J.; Slattery, A.; Basak, A. Nanoscale study of clausenthalite-bearing symplectites in Cu-Au-(U) ores: Implications for ore genesis. *Minerals* **2018**, *8*, 67. [[CrossRef](#)]
58. Meldrum, A.; Boatner, L.A.; Weber, W.J.; Ewing, R.C. Radiation damage in zircon and monazite. *Geochim. Cosmochim. Acta* **1988**, *62*, 2509–2520. [[CrossRef](#)]

